**Marisa Montoya · Alexa Griesel · Anders Levermann
Juliette Mignot · Matthias Hofmann
Andrey Ganopolski · Stefan Rahmstorf**

The earth system model of intermediate complexity CLIMBER-3α. Part I: description and performance for present-day conditions

Abstract We herein present the CLIMBER-3α Earth System Model of Intermediate Complexity (EMIC), which has evolved from the CLIMBER-2 EMIC. The main difference with respect to CLIMBER-2 is its oceanic component, which has been replaced by a state-of-the-art ocean model, which includes an ocean general circulation model (GCM), a biogeochemistry module, and a state-of-the-art sea-ice model. Thus, CLIMBER-3α includes modules describing the atmosphere, land-surface scheme, terrestrial vegetation, ocean, sea ice, and ocean biogeochemistry. Owing to its relatively simple atmospheric component, it is approximately two orders of magnitude faster than coupled GCMs, allowing the performance of a much larger number of integrations and sensitivity studies as well as longer ones. At the same time its oceanic component confers on it a larger degree of realism compared to those EMICs which include simpler oceanic components. The coupling does not include heat or freshwater flux corrections. The comparison against the climatologies shows that CLIMBER-3α satisfactorily describes the large-scale characteristics of the atmosphere, ocean and sea ice on seasonal timescales. As a result of the tracer advection scheme employed, the ocean component satisfactorily simulates the large-scale oceanic circulation with very little numerical and explicit vertical diffusion. The model is thus suited for the study of the large-scale climate and large-scale ocean dynamics. We herein describe its performance for present-day boundary conditions. In a companion paper (Part II), the sensitivity of the model to variations in the external forcing, as well as the role of certain model parameterisations and internal parameters, will be analysed.

1 Introduction

As summarised by Claussen et al. (2002), the success achieved during the last decades in modelling the individual components of the Earth System (atmosphere, ocean, cryosphere and biosphere) prompted efforts to build up models of the Earth System by coupling the state-of-the-art models of the individual components, i.e., general circulation models (GCMs). This led to the development of coupled GCMs, which have been able to describe many details of the present climate and are indispensable tools for the study of variability up to interdecadal timescales, as well as for climate-change assessment within the next centuries. Yet, due to their very high computational cost, the use of such comprehensive models suffers from important limitations, even with using the most powerful computers. Both the length of simulations and the capability to perform sensitivity studies, required to assess the uncertainty surrounding some of the parameters used in climate models, are severely limited.

At the other end of the spectrum of complexity are conceptual models, which aim at providing insight into the specific processes relevant to climate. In these models, all processes which are not directly related to the one studied, but which nevertheless might be important for the global climate system response, are neglected or parametrised.

In the last decade, an attempt to overcome the gap between simple and comprehensive models has come from models of intermediate complexity or so-called

M. Montoya (✉)
Dpto. Astrofísica y Ciencias de la Atmósfera, Facultad de Ciencias Físicas, Universidad Complutense de Madrid, 28040 Madrid, Spain
E-mail: mmontoya@fis.ucm.es
Tel.: +34-91-3944468
Fax: +34-91-3944635

A. Griesel · A. Levermann · J. Mignot · M. Hofmann
A. Ganopolski · S. Rahmstorf
Potsdam Institute for Climate Impact Research, Potsdam, Germany

Earth System Models of Intermediate Complexity (EMICs) (see review by Claussen et al. (2002)). Such models describe a considerable number of processes and feedbacks in the climate system, often including more components than most coupled atmosphere–ocean GCMs (AOGCMs), but due to their low spatial resolution and simplified governing equations, they are computationally less expensive. This makes them suitable for long-term simulations of climate system dynamics, transient palaeoclimate studies, and ensemble runs to perform sensitivity studies to assess the uncertainty in model features such as internal parameters, parametrisations, and forcing, including future greenhouse scenarios.

We have gone one step further in the development of one such EMIC, CLIMBER-2 (Petoukhov et al. 2000), by replacing its oceanic component by a state-of-the-art ocean model. The resultant model is called CLIMBER-3α, indicating it is the first version of the new generation CLIMBER-3 model, currently under development. Owing to its relatively simple atmospheric component, it is up to two orders of magnitude faster than coupled GCMs with horizontal resolution of about 3.5° allowing the performance of a much larger number of integrations and sensitivity studies as well as longer ones. At the same time its oceanic component confers on it a larger degree of realism compared to those EMICs which include simpler oceanic components. The model is thus suited for the study of the large-scale climate and ocean dynamics.

The main motivation behind this effort is the crucial role played by the ocean circulation in the Earth's climate, as highlighted in the past decade by a wealth of studies. In the North Atlantic, the maximum northward heat transport by the ocean is about 1 PW (Ganachaud and Wunsch 2000), contributing to northwest Europe's mild climate (Manabe and Stouffer 1988; Rahmstorf and Ganopolski 1999). There is a clear evidence that the ocean circulation has been different in the past, and that this has in turn influenced the global climate (see Rahmstorf (2002) and references therein). Much insight into the role of the ocean in climate relies on EMICs which contain a simplified representation of the ocean (Petoukhov et al. 2000; Stocker et al. 1992). Thus, it is important to reassess the conclusions attained with models which include more realistic oceanic components. Such an approach based on coupling a comprehensive ocean GCM (OGCM) to a relatively simpler atmosphere has already been followed by other groups, such as in the UVIC model (Weaver et al. 2001) or the ECBILT-CLIO model (Opsteegh et al. 1998; Goose and Fichefet 1999). The UVIC model consists of an energy and moisture balance atmospheric model including dynamical feedbacks coupled to a thermomechanic sea-ice model and to version 2.2 of the GFDL OGCM (MOM 2). ECBILT-CLIO includes a quasi-geostrophic three-dimensional atmospheric model with three layers in the vertical coupled to the CLIO ocean model, which includes a thermodynamic–dynamic sea-ice model and a

comprehensive OGCM. Finally, CLIMBER-3α, as described below (Sect. 2), includes CLIMBER-2's statistical-dynamical atmospheric model coupled to a thermodynamic–dynamic sea-ice model and to GFDL's MOM 3.

We herein present the CLIMBER-3α model by describing its components (Sect. 2) and its performance for present-day boundary conditions (Sect. 3). Finally we draw the main conclusions (Sect. 4). In a companion paper (Part II), we will describe its sensitivity to variations in the external forcing, including changes in the atmospheric CO_2 concentration, and in solar luminosity and volcanism in the last millennium. Also, we will address the role of model features such as resolution and the tracer advection scheme, both in terms of the model performance for the present-day climate and its sensitivity.

2 Model description

The CLIMBER-3α model results mainly from replacing the oceanic component of the CLIMBER-2 EMIC by a state-of-the-art ocean model. Thus, it includes the following modules, all of which are described below: the atmospheric component of CLIMBER-2 (Sect. 2.1), as well as its atmosphere–surface interface and dynamic vegetation module (Sect. 2.2), the atmosphere–ocean coupler (Sect. 2.3), the GFDL MOM 3 OGCM, which has been extended in several ways (Sect. 2.4) and into which a biogeochemistry component has been included (Hofmann et al., unpublished data) and the snow-sea ice model ISIS (Sect. 2.5). For those components which are contained in CLIMBER-2, we focus on the modifications they have undergone for coupling to MOM 3, since their detailed description can be found in Petoukhov et al. (2000).

2.1 Atmospheric component

The atmospheric component of CLIMBER-3α is that of CLIMBER-2, hereafter called POTSDAM-2 (Potsdam Statistical Dynamical Atmospheric Model 2). It is a 2.5-dimensional statistical-dynamical model which includes many of the processes that are also described by more sophisticated GCMs. In contrast to atmospheric GCMs (AGCMs), it does not resolve individual synoptic scale systems, but rather predicts the statistical characteristics connected with ensembles of these systems. However, the large-scale circulation (e.g. the monsoons, jet streams, Hadley circulation) and the main high- and low-pressure areas are explicitly resolved. The model is based on the assumption of a universal vertical structure of temperature and humidity in the atmosphere. This allows reducing the three-dimensional description to a set of two-dimensional, vertically averaged prognostic equations for temperature and humidity. The three-dimensional fields, which

are needed for the calculation of dynamics and of radiative fluxes, can then be obtained by using the vertical profiles. The atmospheric circulation, as well as the energy and moisture transport, are computed at ten pressure levels, while long-wave radiation is calculated using 16 levels. An explicit integration scheme is used. In CLIMBER-3α the horizontal resolution of POTS-DAM-2 was increased to $7.5° \times 22.5°$ instead of $10° \times 51.4°$ as in CLIMBER-2, and the time-step reduced from one to half a day. Our main motivation to double the zonal resolution from CLIMBER-2 was to improve some regional aspects of the fields which were not captured properly, even when the atmospheric model was forced with prescribed SSTs. In particular, the North Atlantic was one of the regions which was poorly simulated. Owing to its importance for the global oceanic circulation and climate, we decided to switch to a somewhat finer resolution in order to achieve a better representation. A more detailed study of the impact of resolution with the results of the original, coarser resolution version of the model ($5° \times 5°$ in the ocean and $10° \times 51°$ in the atmosphere) will be included in part II of this paper.

2.2 Land-surface scheme and terrestrial vegetation module

CLIMBER-3α includes CLIMBER-2's atmosphere-surface interface (ASI) (Petoukhov et al. 2000), which is based on the Biosphere-Atmosphere Transfer Scheme (BATS) (Dickinson et al. 1986). Each model grid box consists of one or several of six surface types: open water, sea ice, trees, grass, bare soil, and glaciers. For each type sub-, near- and surface characteristics, as well as surface fluxes are calculated separately, while taking into account the different surface properties such as the albedo or roughness length. In contrast to CLIMBER-2, the surface albedo over snow is calculated according to the parametrisations of Shine and Henderson-Sellers (1985) and Grenfell and Perovich (1984), and depends on the snow thickness and surface temperature. A two-layer soil model is included. In CLIMBER-3α, runoff is added to the net freshwater flux into the ocean every time-step instead of in an annual mean basis as in CLIMBER-2.

Since a detailed representation of the ocean's bottom topography is required to achieve a realistic representation of the oceanic circulation, the simplified land-mask of CLIMBER-2 was replaced by that obtained by interpolation of the $1/12°$ ETOPO-5 (Earth Topography 5-min) dataset from the World Data Center for Marine Geology & Geophysics at Boulder (National Geophysical Data Center 1988) to the longitudinal resolution of POTSDAM-2. The atmospheric and oceanic grids, despite having different horizontal resolutions, are perfectly congruent, which allows employing a relatively simple interpolation scheme between the two (Sect. 2.3).

A simplified orography based on interpolation and smoothing of the ETOPO-5 Earth's topography is employed (Fig. 1a). The fraction of glaciers was prescribed in agreement with their current location and extension (Fig. 1b). Vegetation cover can either be prescribed or simulated as a function of climate through the VECODE terrestrial vegetation module (Brovkin et al. 2000), in turn affecting climate through characteristics such as the albedo, roughness-length and fraction of surface covered by snow. To keep the model set-up as simple as possible in all simulations described herein, the distribution of vegetation was prescribed from the output of VECODE driven by the Leemans and Cramer (1991) climatology (not shown). However, as in CLIMBER-2, the structure of CLIMBER-3α has been kept modular so that any individual model component can be easily switched on and off, in particular the dynamic vegetation module. Thus, VECODE can easily be used in further studies which will require interactive vegetation, such as palaeoclimate simulations.
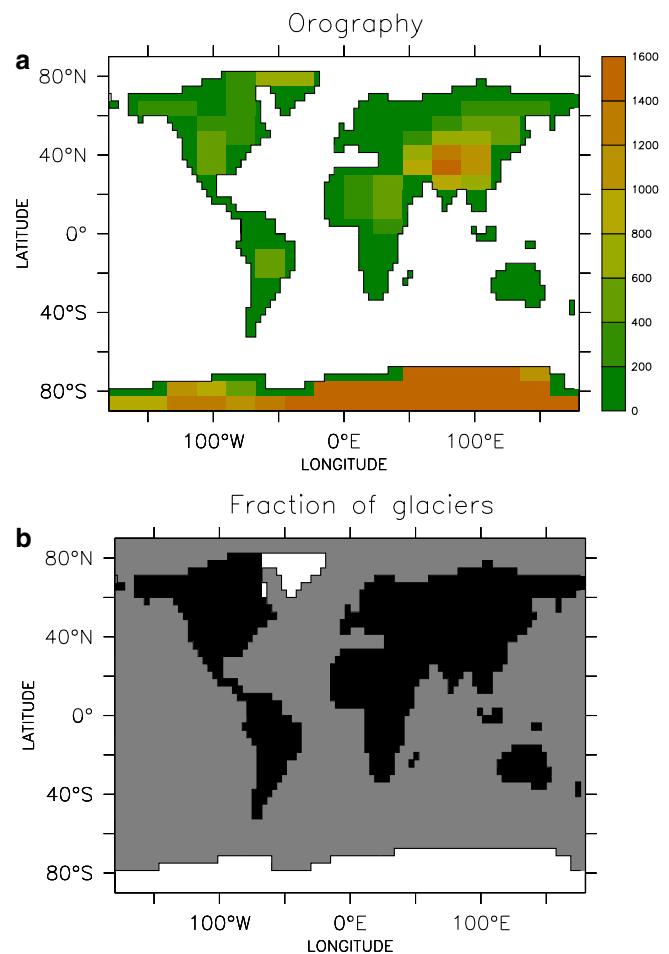
Fig. 1 Prescribed **a** land-orography (in m) and **b** glacier location in the atmospheric grid ($7.5° \times 22.5°$). Note that an atmospheric grid cell can overlie partly land and partly ocean; the model's land-mask is shown

2.3 Atmosphere–ocean coupler

The atmospheric and oceanic components of CLIM-BER-3α are coupled via heat, freshwater and momentum fluxes. The atmosphere–ocean fluxes are calculated separately for sea ice and leads. Fluxes are exchanged with a time-step of half a day. The coupler employs the same horizontal resolution as the ocean model (i.e. 3.75°×3.75°). The individual fluxes which contribute to the heat, freshwater or momentum fluxes are either calculated by the atmosphere or the ASI or by the coupler (see below). In the first two cases (that is, for liquid precipitation, snow, net absorbed short-wave radiation and downwelling long-wave radiation), the fluxes are interpolated to the coupler's resolution; in the third case (basically for the calculation of the outgoing long-wave radiation and turbulent heat fluxes), the coupler makes use of the variables required from each module (such as the surface–air temperature (SAT) and relative humidity, SST, sea-ice thickness and concentration, etc.) and interpolates these to its resolution to calculate the fluxes in its own grid. Variables are interpolated bi-linearly, whereas for the fluxes a conservative interpolation scheme was employed in order to guarantee heat and mass conservation. The latter consists of two piecewise linear conservative interpolations performed first in the longitudinal and then in the latitudinal direction. On each dimension, the scheme proceeds first by assigning values at the borders of each (coarse) grid cell of the field to be interpolated. These are in principle arbitrary; in practice, the mean of the field values on the two neighbour grid cells was chosen. The value of the field at the centre is calculated by imposing conservation, assuming a linear function between the centre and each of the two borders. Finally, the values of the field on the finer mesh are obtained by interpolating linearly between the borders and the central value. By construction the interpolation is conservative. The coupling procedure does not include any flux corrections for heat and freshwater fluxes, but for the momentum-flux the anomalies relative to the control run are computed and added to climatological data (see below).

The atmosphere–ocean heat flux is given by the sum of the radiative (downward long-wave radiation and net solar radiation at the surface) and turbulent fluxes (sensible and latent heat fluxes). The downward long-wave radiation and the solar radiation absorbed at the surface by the sea ice and leads are calculated by the atmospheric module taking into account the albedo for each surface type, while the upward long-wave radiation and the turbulent heat fluxes are calculated by the coupler by means of the same bulk equations employed in CLIMBER-2.

In contrast to CLIMBER-2, snow is allowed to accumulate over sea ice. This mechanism appears to play an important role especially in Antarctic sea-ice, where the ice-pack is thin and partly covered by perennial snow, due to its effect on snow-ice formation and its insulating effect, which retards or prevents summer melt

and winter growth and thereby affects the seasonal cycle of the sea-ice cover (Fichefet and Morales-Maqueda 1999; Massom et al. 2001). As for snow over land (Sect. 2.1), the surface albedo over sea ice and snow is calculated according to the parametrisations of Shine and Henderson-Sellers (1985) and Grenfell and Perovich (1984), and depends on the sea-ice and the snow thickness and surface temperature.

The penetration of short-wave radiation into the water column as well as into sea ice is taken into account. In the latter case, the fraction of short-wave radiation penetrating through the surface of the snow-ice system depends on the presence of snow and on cloudiness. If snow is present, short-wave radiation does not penetrate the surface of the snow-ice system. Over bare ice, the transmission coefficient (as well as the albedo) is smaller under clear sky, as downwelling solar radiation has a larger long-wave component, which is rapidly absorbed at the surface (Grenfell and Maykut 1977).

In contrast to most ocean models, MOM 3 includes an explicit free-surface, which allows for the coupling of the atmosphere and ocean directly via freshwater fluxes (see Sect. 2.4). The atmosphere–ocean freshwater flux is given by the sum of precipitation, evaporation, runoff and calving. Precipitation (liquid or in the form of snow) is calculated by the atmosphere. Evaporation is calculated by the coupler, assuming zero evaporation over sea ice. Runoff and calving are calculated by the ASI. Calving arises from the fact that a maximum amount of 1 m of snow in water equivalent is allowed to accumulate over land, the excess being transferred to the ocean via the runoff scheme. In the future, it is planned to couple a continental ice-sheet model. In addition, the freshwater flux due to sea-ice formation or melting and the salt flux associated with brine rejection, calculated by the sea-ice component (Sect. 2.5), are included.

Several authors have demonstrated the large sensitivity of the ocean circulation to the wind-stress field employed (Timmermann and Goosse 2004; Oke et al., unpublished data). Owing to the coarse atmospheric resolution employed and due to the deficiencies in the atmospheric dynamics, the wind-field simulated by the atmospheric module is not satisfactory to force the ocean. As shown in Fig. 2, the main discrepancy between the simulated and the NCEP/NCAR reanalysis wind-stress climatologies (Kistler et al. 2001) is found over the North Atlantic, where deficiencies in the sea-level pressure (SLP) field (Sect. 3.1) lead to an inadequate representation of the subpolar gyre. As a result, forcing the model with interactive winds results in no North Atlantic Deep Water (NADW) formation. Thus, we have preferred to sacrifice full coupling of the model for the sake of a reasonable oceanic circulation. The approach employed was to force the model with the 50-year (1948–1997) NCEP-NCAR reanalysis wind-stress climatologies plus the wind-stress anomalies computed by the model relative to the control run. This correction introduces some feedback between the ocean and the
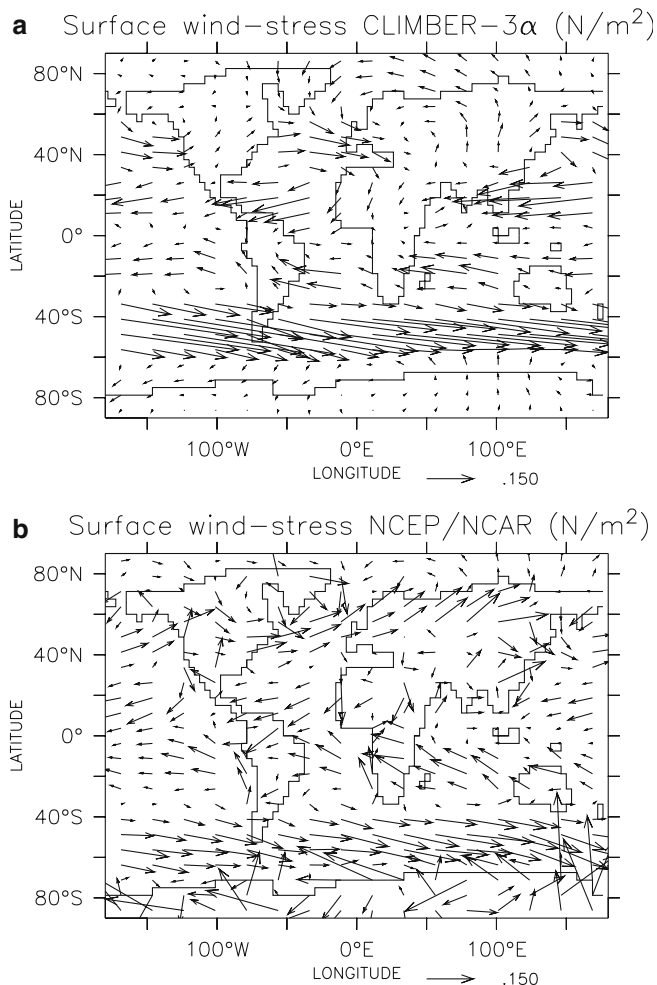
Fig. 2 Mean annual wind-stress **a** simulated in the control run by the model and **b** in the NCEP/NCAR climatology (in Nm^{-2})

anomalies of wind-stress, while still ensuring a realistic mean wind stress. Note that only the control run is described in the present study (Sect. 3), where the correction to the winds vanishes by definition. It must be kept in mind that this anomaly approach applies exclusively to the wind-stress used to force the ocean; within the atmosphere the advection of heat and moisture is carried out entirely by the simulated winds.

2.4 Oceanic component

The oceanic component of CLIMBER-3α is the MOM 3 ocean model developed at the Geophysical Fluid Dynamics Laboratory (GFDL) in Princeton (Pacanowski and Griffies 1999), to which a number of new parametrisations and numerical schemes have been added (Hofmann and Morales-Maqueda, unpublished data). It is a primitive equation, three-dimensional OGCM. It employs a staggered Arakawa B-grid (Arakawa 1966; Bryan 1969) with a horizontal resolution of $3.75° \times 3.75°$ and a z-coordinate vertical discretisation with 24 vari-

ably spaced levels, ranging from 25 m thickness at the surface to ca. 500 m at depth, allowing for partial cells. The topography is based on the 1/12° ETOPO5 dataset (National Geophysical Data Center 1988).

One main difference with respect to previous MOM versions is the fact that MOM 3 includes a non-linear, explicit free-surface such that the ocean volume changes directly via explicit freshwater fluxes, and changes in ocean volume are directly incorporated into the tracer equations. This allows accounting for the effect of freshwater fluxes on the ocean's buoyancy field (Griffies et al. 2000a, b).

The model makes use of the asynchronous time-stepping technique by Bryan (1984), wherein, in order to accelerate the convergence of the model to equilibrium, the momentum and the tracer equations are integrated asynchronously and with different time-steps. However, when used in combination with a non-linear explicit free-surface this method leads to a severe non-conservation of volume, and therefore tracers, resulting from the asynchronous integration of the tracers and the free-surface in the external mode of the momentum equations. The time-stepping was thus modified by splitting the integration of the free-surface and the barotropic mode within the external mode, integrating the tracers and the free-surface synchronously on one hand (with time-steps of 43,200 s and ca. 982 s respectively) and the baroclinic and barotropic transports on the other (with time-steps of 3,600 s and ca. 82 s) (Hofmann and Morales-Maqueda, unpublished data).

The penetration of short-wave radiation into the water column is taken into account as a source term for the ocean temperature following an exponential law.

The model uses horizontal Laplacian friction, with a latitude-dependent horizontal viscosity, v_v, ranging from $0.1–3.2 \times 10^5$ m^2 s^{-1} and a constant vertical viscosity of $v_v = 10 \times 10^{-4}$ m^2 s^1. With such values of the horizontal viscosity, the Munk boundary layer is only resolved with one point. Griffies et al. (2000b) demonstrated that this leads to spurious mixing for several advection schemes. However, we believe that this effect is probably weak in our case since we apply an advection scheme with negligible numerical diffusion (Prather (1986), see below). The reader is referred to Hofmann and Morales-Maqueda (unpublished data) for an extensive discussion on the implementation, performance and diagnosis of numerical diffusion of the Prather 1986 advection scheme in MOM 3 and its comparison to other advection schemes such as FCT (Gerdes et al. 1991), upstream and quicker.

Mixing of tracers is accomplished via Laplacian isopycnal diffusion (Redi diffusion) (Redi 1982) with a constant isopycnal diffusivity coefficient $\kappa_h = 1,000$ m^2 s^{-1}. The skew-flux approach of the Gent–McWilliams (1990) parametrisation of advection of tracers by eddies (1990; Gent et al. 1995; Griffies 1997) was included, with a constant thickness-diffusivity of $\kappa_{thk} = 250$ m^2 s^{-1}.

A non-constant vertical diffusivity not available in the original MOM 3 code (hereafter Hasumi-Ledwell), with vertical mixing coefficients enhanced over rough topography (Hasumi and Suginohara 1999) and dependent on the stratification of the water column, following a model for the internal wave energy source strength (Ledwell et al. 2000) was employed (Fig. 3):

$$\kappa_v(z) = \kappa_v^{bg} + \frac{Ar}{[1 + \alpha(\rho(z_r) - \rho(z))]^2}, \tag{1}$$

where κ_v^{bg} is the background vertical diffusivity, A and α are constants, $r = \sigma_h/h$ is the normalised roughness of topography h, ρ is the potential density, and z_r is a reference depth. The values employed in the current version are:

$$A = 10 \times 10^{-4}\,\mathrm{m^2 s^{-1}} \quad \alpha = 12\,\mathrm{m^3\,kg^{-1}}, \tag{2}$$

while z_r is the bottom depth. This gives vertical diffusivity values ranging from 0.1×10^{-4} m^2 s^{-1} for the ocean interior to 10×10^{-4} m^2 s^{-1} above rough bottom topography. In addition, the KPP (K-profile parametrisation) boundary layer mixing scheme of Large et al. (1994) is used.

In recent years direct and indirect measurements of mixing coefficients have revealed that diapycnal mixing is highly variable in space and time, with values ranging from below $\kappa_v = 0.1 \times 10^{-4}$ m^2 s^{-1} in the ocean interior (Gregg et al. 2003; Ledwell et al. 1993; Moum and Osborn 1986; Oakey et al. 1994) to $\kappa_v = 100 \times 10^{-4}$ m^2 s^{-1} near highly variable bottom topography or along continental slopes (Ledwell et al. 2000; Moum et al. 2002; Polzin et al. 1997). These results indicate the high level of uncertainty surrounding the values of abyssal vertical diffusivity. For this reason, we have decided to employ two different values for the background vertical diffusivity coefficient ($\kappa_v^{bg} = 0.1$,

0.4×10^{-4} m^2 s^{-1}) in all the simulations shown herein and to perform a control run for each of the two (hereafter VD01 and VD04, respectively). The focus will be mainly on VD01 and the differences between VD04 and VD01 whenever they are significant. Although when compared to the $\kappa_v \leq 0.1 \times 10^{-4}$ m^2 s^{-1} values inferred for the ocean interior, a value such as $\kappa_v = 0.4 \times 10^{-4}$ m^2 s^{-1} appears too high, diffusion values for a coarse-resolution model might not necessarily be the same or directly comparable to observed turbulent diffusion. In addition, such higher values allow a better comparison of our results in terms of oceanic fields such as the meridional overturning circulation (MOC) or the heat transport by the ocean with previous ocean model simulations, most of which we believe employ higher values of both explicit and numerical diffusivity (see Sects. 3.3, 4).

The convective scheme employed is a simplified version of the Paluszkiewicz and Romea (1997) scheme which was not in the original MOM 3 code. The idea behind this parametrisation is that convection occurs in very narrow water columns, or plumes (Marshall and Schott 1999) with spatial scales ≤ 1 km, thus well below the resolution of coarse ocean models. Usual convective schemes are based either on the application of very high mixing coefficients when the water column becomes unstably stratified or on actual mixing of the water column, resulting in mixing of the whole grid-cell area, and therefore on too large spatial scales. The parametrisation employed here attempts to simulate individual convective plumes at a given grid-cell, allowing for mixing well before the whole water column is destabilised. For this purpose the grid cells are assumed to be divided vertically into slices; if the vertical density stratification turns out to be unstable, then the uppermost slice is taken down to a level of neutral buoyancy and the slices above this level are shifted upward and remixed. In this way, a minimum amount of mixing is achieved in order to stabilise the vertical stratification of the water column.

The advection of momentum employs a second-order centred differences scheme. The advection of tracers employed was not in the original MOM 3 code, but is that of Prather (1986). It is a positive definite, second-order moments conserving scheme with very little numerical diffusion. It has been used in many tracer transport models as well as in atmospheric models such as the GISS Model II (Hansen et al. 1983). It is also the original advection scheme of the sea-ice model employed in CLIMBER-3α (Sect. 2.5). Our wish to assess the role of vertical diffusivity in the MOC was the main motivation for employing this scheme. This required a tracer advection scheme with as little numerical diffusion as possible. The Prather (1986) advection scheme follows the upstream method, but applied to all moments to second order. In this way, the adverse effects of numerical diffusion with which most advection schemes used in ocean models are beset are removed. The scheme leads to a signifi-
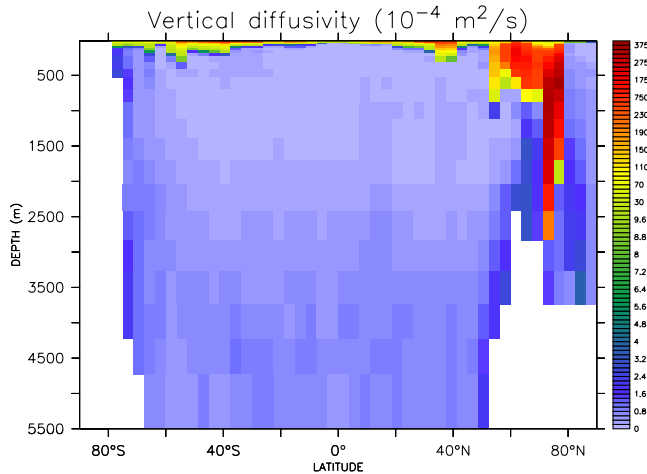
Fig. 3 Vertical diffusivity employed in CLIMBER-3α for a background value of $\kappa_v^{bg} = 0.1 \times 10^{-4}$ m^2 s-1, zonally averaged over the global ocean (in 10^{-4} m^2 s^{-1})

Fig. 4 a, c Zonally averaged planetary albedo and **b, d** outgoing long-wave radiation at the top of the atmosphere (in Wm^{-2}) for December to February (**a, b**) and June to August (**c, d**). CLIMBER-3α: *black*, CLIMBER-2: *red*, ERBE data: *green*
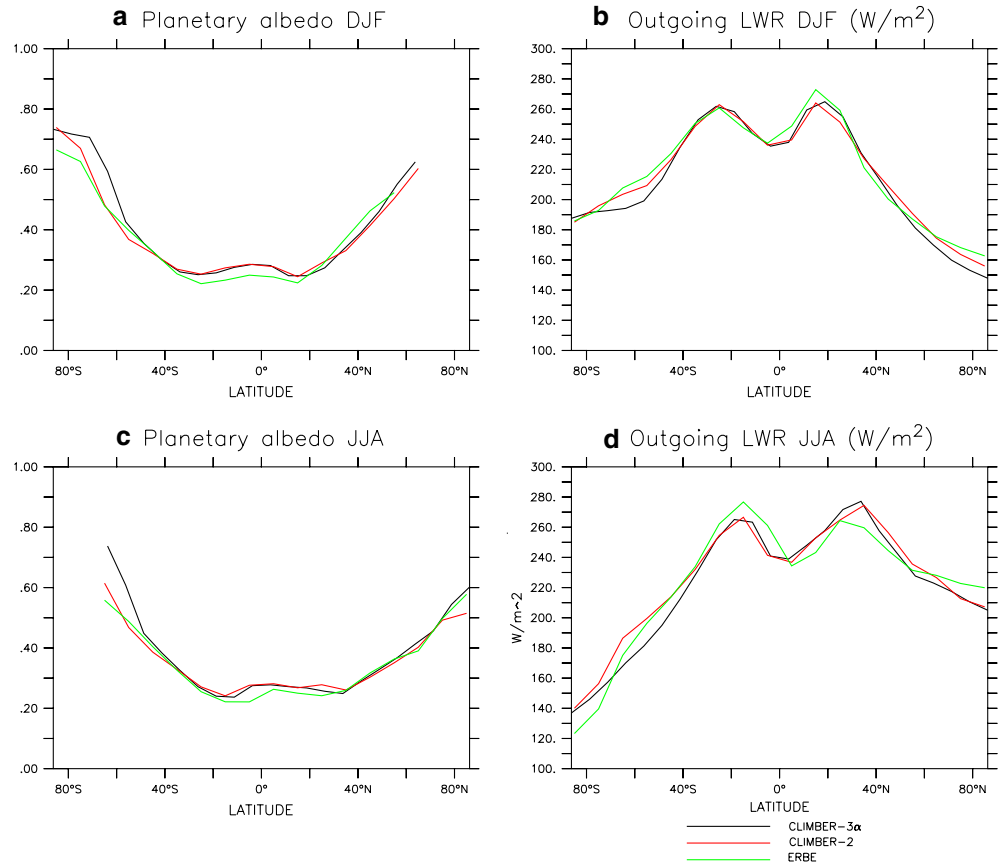

cant improvement in the representation of water masses, notably the Antarctic Intermediate Water and the Atlantic layer in the Arctic Ocean (Hofmann and Morales-Maqueda, unpublished data). As a consequence, it also allows for a better simulation of the circulations. For example, deep water formation in the Greenland-Iceland-Norwegian (GIN) Seas and its overflow over the Greenland-Iceland-Scotland ridge are represented, and thus even with very low explicit vertical diffusion, the large-scale oceanic circulations are reproduced (Sect. 3.3). In contrast, when traditional tracer advection schemes are used, the representation of water masses worsens, the GIN Seas overflow disappears, and the Atlantic overturning circulation worsens or even disappears (Hofmann and Morales-Maqueda 2005, unpublished data). Under these circumstances, a reasonable Atlantic overturning circulation can only be attained by employing high values of vertical diffusivity, thus artificially correcting a model failure by tuning a parameter. This will be illustrated in part II when the results of using Prather (1986) compared to other advection schemes are shown. We believe that many coarse OGCMs, which employ tracer advection schemes with high numerical diffusion, indeed need to resort to high values of the explicit vertical diffusion in order to achieve a satisfactory representation of the Atlantic overturning circulation.

2.5 Sea-ice component

The sea-ice model is the Ice and Snow Interfaces (ISIS) model developed at the Institut d'Astronomie et de Géophysique Georges Lemaître at Louvain-la-Neuve (Fichefet and Morales-Maqueda 1997), also included in the CLIO model from that institution (Goose and Fichefet 1999). It is a two-dimensional (latitude–longitude) thermodynamic-dynamic model with one layer of ice and one layer of snow. As in the ocean model (Sect. 2.4), it uses a horizontal staggered Arakawa B-grid with a resolution of 3.75°×3.75°. The thermodynamics is an improved version of Semtner (1976). It takes into account the heat capacity of snow and ice, the thermodynamic effects of the sub-grid-scale snow and ice thickness distributions, the storage of latent heat in brine pockets, and the formation of snow ice. It accounts for the presence of sea-ice, snow and leads. The sea-ice dynamics allows the sea ice to flow under the effect of winds and currents and to self-interact, deforming. The dynamics employs an elasto-visco-plastic rheology formulation (Hunke and Dukowicz 1997), thereby conserving mechanical energy. This scheme represents a modification of the standard Hibler (1979) visco-plastic rheology, where sea-ice is allowed to flow plastically for normal strain rates and to deform in a linear viscous manner for very small strain rates. As in

Fig. 5 a, c Zonally averaged
surface–air temperature (SAT)
(in °C) and **b, d** precipitation (in
mm/day) for December to
February (**a, b**) and June to
August (**c, d**). CLIMBER-3α:
black, CLIMBER-2: *red*,
NCEP/NCAR data: *green*
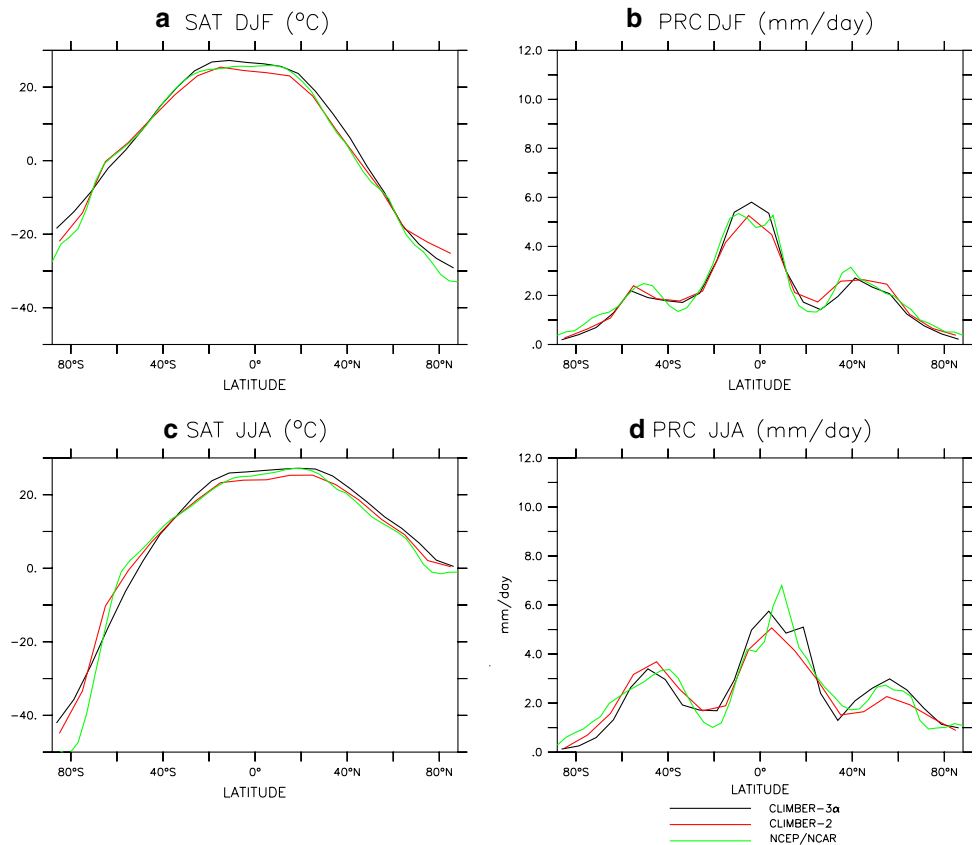
the ocean model (Sect. 2.4), the advection scheme is that
of Prather (1986).

3 Performance for present-day boundary conditions

This section discusses the performance of the CLIM-
BER-3α model for "present-day" (preindustrial)
boundary conditions, namely: the present-day Earth
geography and ice-sheet distribution (Fig. 1), vegetation
(disregarding land-use changes due to human activities),
insolation and atmospheric CO_2 concentration
(280 ppmv).

Since the ocean component is computationally the
most expensive, there is no gain in performing a spin-up
of the ocean model to equilibrium separately and then
coupling it with the atmosphere. Thus, the fully coupled
model was integrated for 5,000 years. The ocean model
was initialised with zero velocities, no sea ice, and Lev-
itus (1982) temperatures and salinities. In the atmo-
sphere the temperature and specific humidity were
initially set to zero.

After 5,000 years, only the global deep ocean circu-
lation still shows a small drift (less than 0.07 Sv/century,
not shown). The Atlantic overturning also shows some
weak variability (less than 0.5 Sv, not shown) due to
oscillations of a few grid points in the deep convection
area. We recall that CLIMBER-3α is not designed to

simulate the internal short-term variability, but only the
mean climate.

We show 10-year averages of the atmospheric fields
(Sect. 3.1), atmosphere–ocean fluxes (Sect. 3.2), oceanic
fields (Sect. 3.3), and sea-ice fields (Sect. 3.4) at the end
of the integration.

3.1 Atmospheric fields

The zonally averaged atmospheric fields simulated by
CLIMBER-3α are practically indistinguishable from
those simulated by CLIMBER-2. As an example, Fig. 4
compares the zonally averaged planetary albedo as well
as the outgoing long-wave radiation at the top of the
atmosphere (OLR) simulated by CLIMBER-3α with the
Earth Radiation Budget Experiment (ERBE) data
(Harrison et al. 1990), in December to February (DJF)
and June to August (JJA). Also shown for comparison
are the results with CLIMBER-2 (Petoukhov et al.
2000). The CLIMBER-3α results are very similar to
those with CLIMBER-2, both showing a good agree-
ment with the observations. As with CLIMBER-2, the
differences between the observed and simulated OLR are
below 20 Wm^{-2}, an error typical for atmospheric
GCMs. Consistent with its higher SAT (see below),
VD04 shows a somewhat lower planetary albedo and
higher OLR than VD01 in JJA over mid-latitudes, thus
agreeing even better with the data (not shown). The
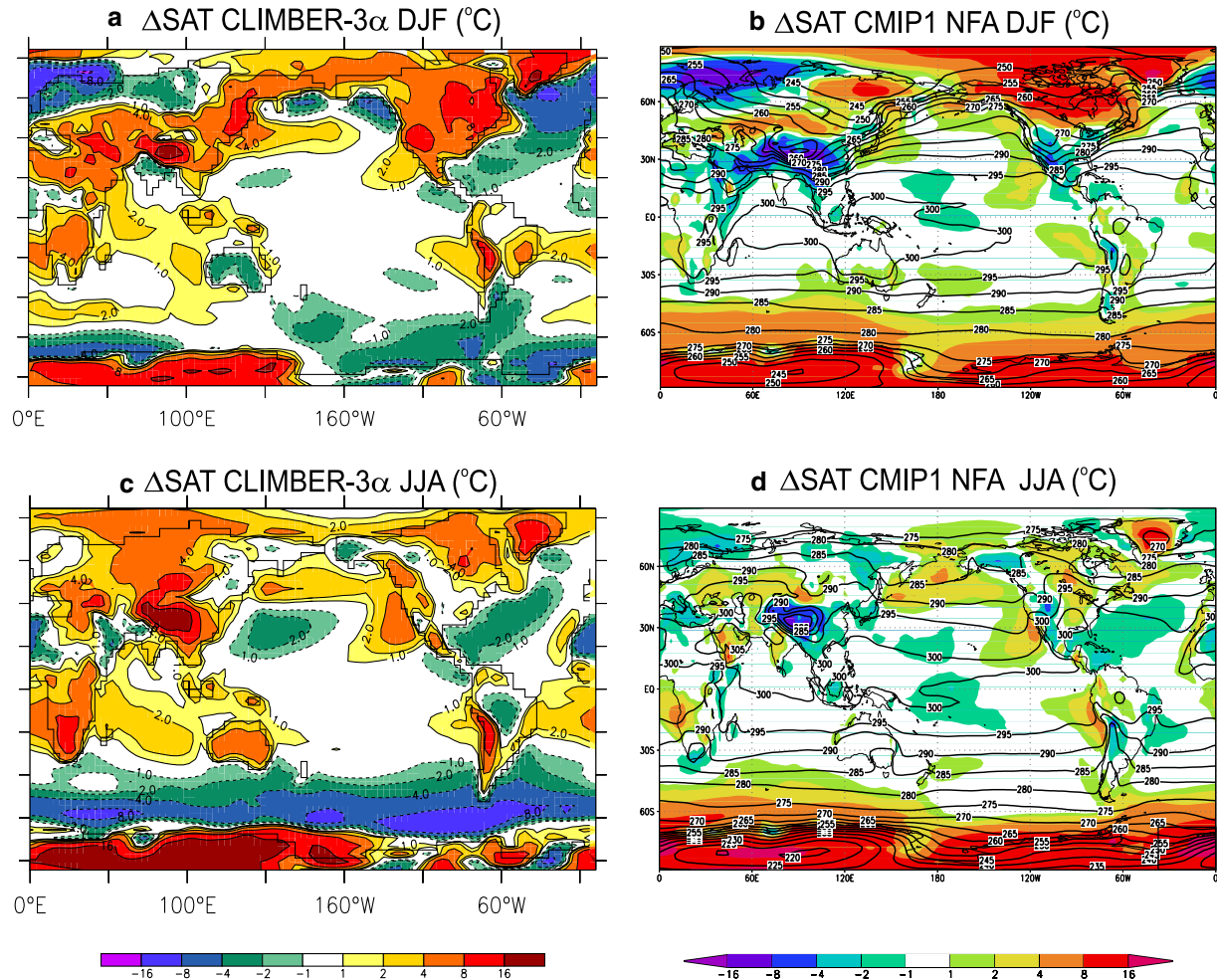
Fig. 6 Mean SAT differences between the control run and the NCEP–NCAR climatology (model minus data) **a** in December to February, and **c** in June to August, and between the average of all CMIP1 (Lambert and Boer 2001) non-flux adjusted model control runs and the data (*shaded*) **b** in December to February, and **d** in June to August. Also shown (*contours*) is the climatologically simulated SAT (in °C)

horizontal distribution of the planetary albedo and OLR (not shown) reveal that the largest biases in these fields, relative to the climatologies, can be attributed to biases in the sea ice and cloud cover. The model overestimates the cloud concentration at mid and high latitudes in both hemispheres both in DJF and JJA (not shown) and the sea-ice extent in the Southern Hemisphere throughout the year and in the Arctic in DJF (Sect. 2.5). Because of the high albedo of clouds and sea ice, both features lead to an overestimation of the planetary albedo at high latitudes (Fig. 4). In addition, because the presence of high clouds leads to lower emission temperatures, in the tropics the OLR is anticorrelated with the cloud distribution. Thus, many of the biases of the OLR field can be attributed to biases in the cloud field (not shown). Basically, the monsoons are underestimated both in winter and summer leading to an underestimation of the cloud cover and thus to an overestimation in the OLR. In the same way, the dry conditions in subtropical areas are also underestimated, leading to too high cloud

concentrations and too low values of the OLR. Since these biases can be identified with deficiencies in the simulation of precipitation, improving the precipitation could improve the OLR field as well.

Figure 5 shows the zonally averaged SAT and precipitation for DJF and JJA. Again, the results by CLIMBER-3α are very similar to those with CLIMBER-2 and compare satisfactorily with the data. The largest discrepancies concerning the SAT field is an overestimation at high latitudes, with the largest biases found at high southern latitudes. Figure 6a, c shows the difference between the SAT simulated by the model in VD01 and the NCEP–NCAR reanalysis (Kistler et al. 2001) for DJF and JJA. The largest discrepancies are found at high latitudes and over the centre of the continents, which are too warm all-year round, as well as over the North Atlantic and Southern Ocean, which are too cold, especially in the winters. The biases found in the SAT field are very likely the result of a combination of factors. The comparison of the snow-cover field (not
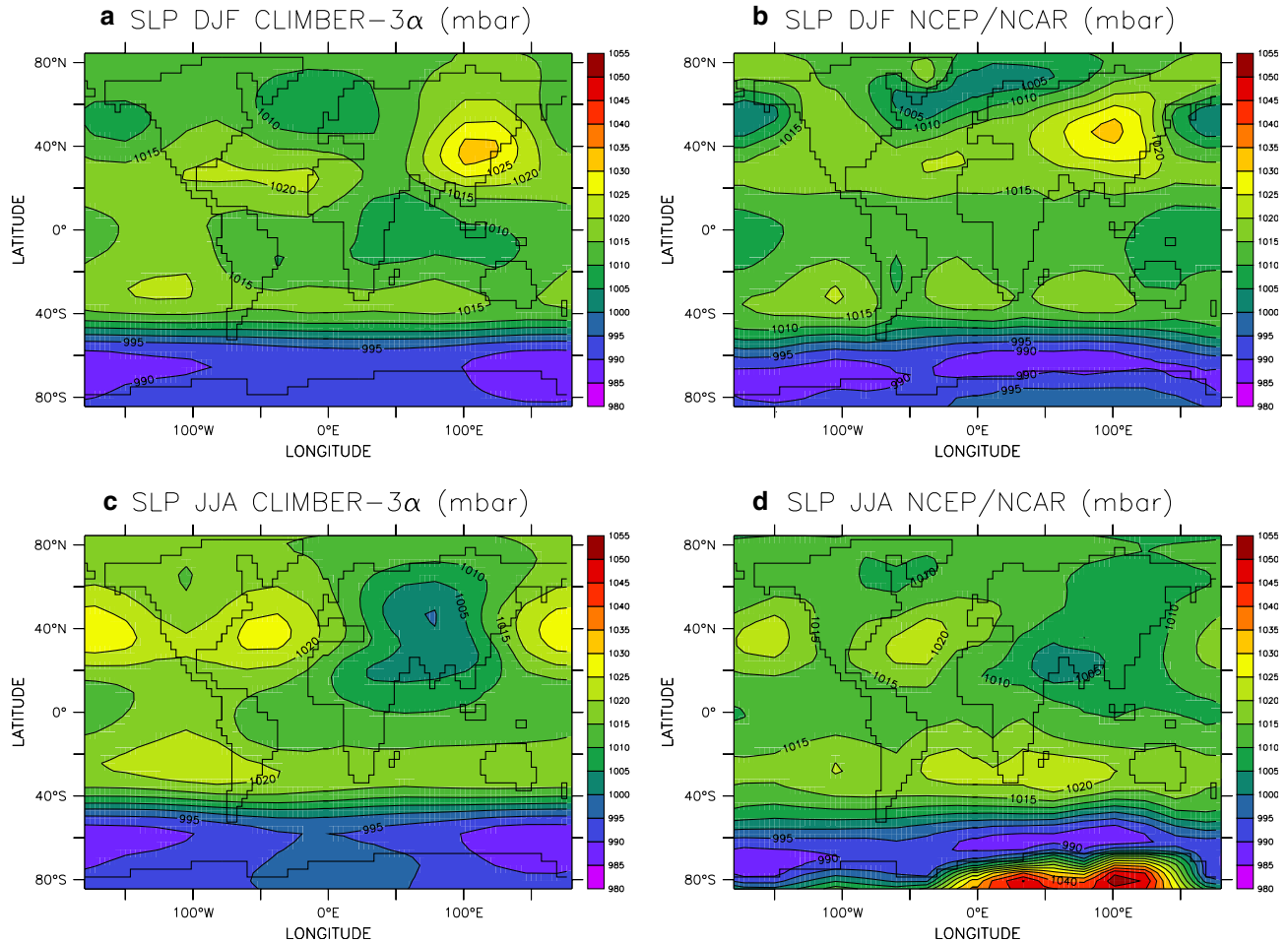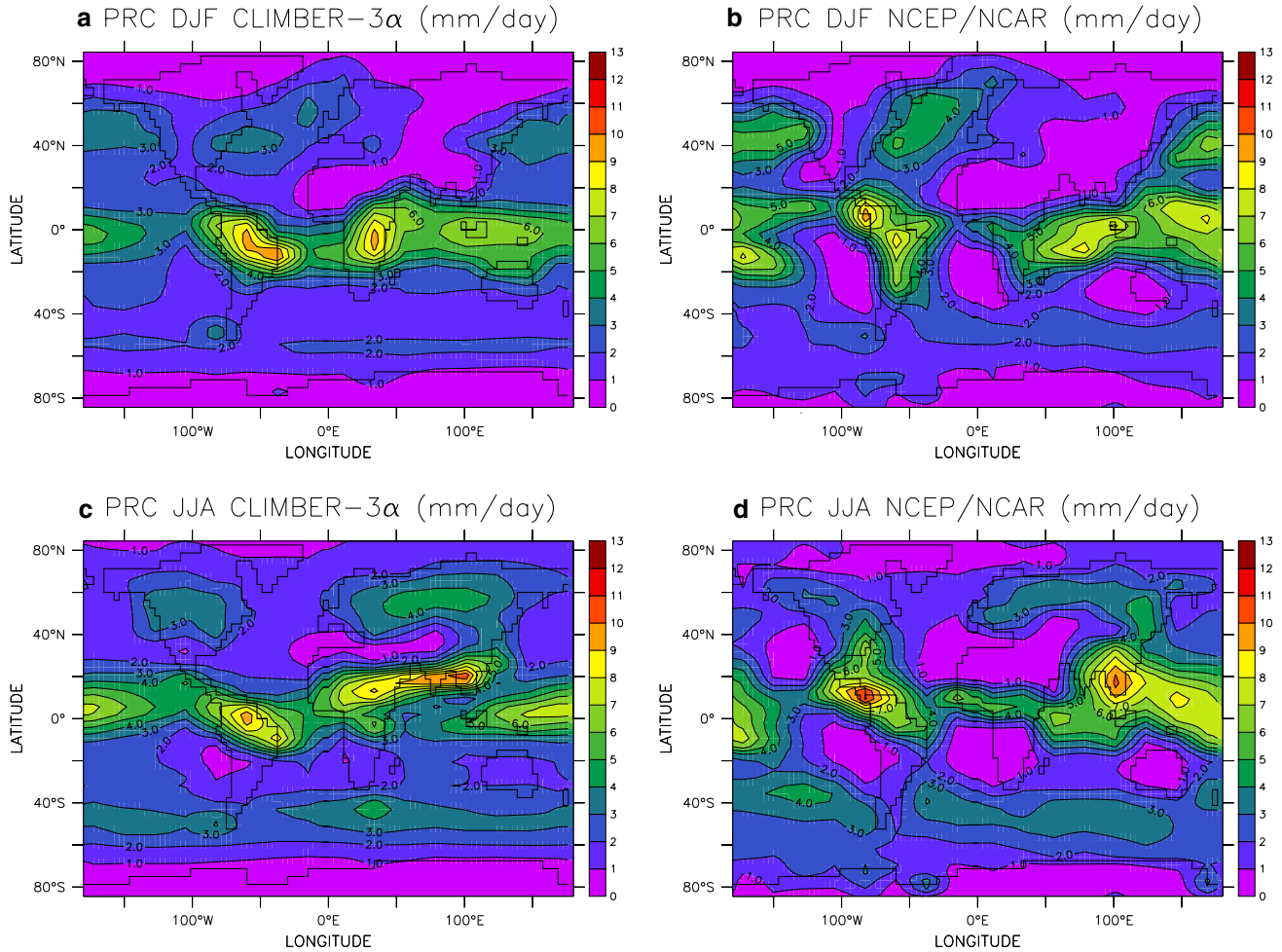
Fig. 7 Mean sea-level pressure (*SLP*) in December to February **a** simulated in the control run by the model and **b** in the NCEP–NCAR climatology, and in June to August **c** simulated in the control run by the model and **d** in the NCEP-NCAR climatology (in mbar)

shown) against the National Oceanic and Atmospheric Administration (NOAA) Special Sensor Microwave/ Imager (SSM/I) snow-cover data (Grody 1991) shows quite a good agreement. However, the model tends to overestimate the snow cover over northern Europe in DJF, which could partly account for the cold temperatures over there. The comparison of the biases in the SAT field with those in the cloud and downwards long-wave radiation (DLWR) distribution (not shown) indicates that the positive SAT biases over the centres of the continents in the extra-tropics and high latitudes (North America, Eurasia, Greenland, South Africa and South America) are associated with overestimation of the concentration of clouds at mid and high latitudes, leading to enhanced trapping of the long-wave radiation emitted by the Earth to the atmosphere (greenhouse effect) and thus to overestimated values of the DLWR.

The low temperatures over the North Atlantic are probably the consequence of too weak northward heat transport by the Atlantic Ocean, associated with deficiencies in the ocean circulation (Sect. 3.3), and an overestimated sea-ice extent (Sect. 3.4), which through the positive sea-ice albedo feedback, further contributes to lower the temperatures. The cold SATs over the

Southern Ocean in JJA are also associated with overestimated sea-ice extent (Sect. 3.4). Both features, and especially the Southern Ocean cold bias, improve slightly for VD04 (not shown), which shows a slightly enhanced meridional overturning circulation and northward heat transport in the Atlantic Ocean, and a year-round reduction of sea-ice in both hemispheres (Sect. 3.4).

The errors found in the SAT field might seem extremely severe. Yet, specially for DJF, they are comparable to those of the average over all non-flux corrected models compiled in the first phase of the Coupled Model Intercomparison Project (CMIP1) (Lambert and Boer 2001) (Fig. 6b, d). Even the patterns are similar. In particular, in DJF the average AOGCM is colder by more than 8°C over Northern Europe, and warmer by more than 8°C over North America and Antarctica. In JJA both CLIMBER-3α and the CMIP1 average non-flux adjusted model show errors above 8°C over Antarctica and Greenland. Given that the average over many models is usually better than most of individual models, CLIMBER-3α's performance is comparable to that of a recent generation of non-flux adjusted models.

Fig. 8 Mean precipitation (*PRC*) in December to February **a** simulated in the control run by the model and **b** in the NCEP–NCAR climatology, and in June to August **c** simulated in the control run by the model and **d** in the NCEP–NCAR climatology (in mm/day)

The horizontal large-scale SLP distribution (Fig. 7) is, as in CLIMBER-2, reasonably captured by the model, in terms of both the positions and amplitudes of the stationary patterns. The model, however, does show some degree of sensitivity regarding the SLP performance with respect to the land-mask distribution; the realistic land-mask in CLIMBER-3α results in some atmospheric grid-cells which in CLIMBER-2 were full land cells now being a mixture of land and ocean, thus, decreasing the land-sea temperature contrast. This results in a slight shift of the SLP patterns compared to CLIMBER-2. Some regional aspects are not properly captured. Notably the location and intensity of the subpolar low in DJF is not reproduced satisfactorily. As a consequence, the surface wind and wind-stress simulated by the model (not shown) in this region, in particular, are not realistic enough to achieve a realistic oceanic circulation. Thus, we decided not to use the simulated wind-stresses directly to force the model, but to use the wind anomaly model described in Sect. 3.

The distribution of precipitation (Fig. 8) is reproduced reasonably well in comparison with the data. The model reproduces the precipitation maxima over the western tropical Pacific, South and Central America and their seasonal shift following that of the intertropical convergence zone (ITCZ). The intensification of precipitation over southeast Asia in JJA associated with the summer southwest monsoon is also captured. The model captures the secondary precipitation maxima over the North Atlantic and North Pacific oceans in DJF and over North America, Eurasia and the Southern Ocean mid-latitudes in JJA. Yet, there are also important deficiencies: the spatial structure of the low-latitude maxima is not identical to that in the observations, the precipitation maximum around the ITCZ is too broad, the subtropical belt of low precipitation in the Southern Hemisphere is underestimated, especially in the Southern Hemisphere in DJF, and the precipitation maxima over the storm-track areas are underestimated.

The zonally averaged atmospheric circulation is shown in Fig. 9. As CLIMBER-2 (Petoukhov et al. 2000), CLIMBER-3α captures the positions, intensities, and seasonal variations of the jet streams, the tropical easterlies, and the three atmospheric cells reasonably
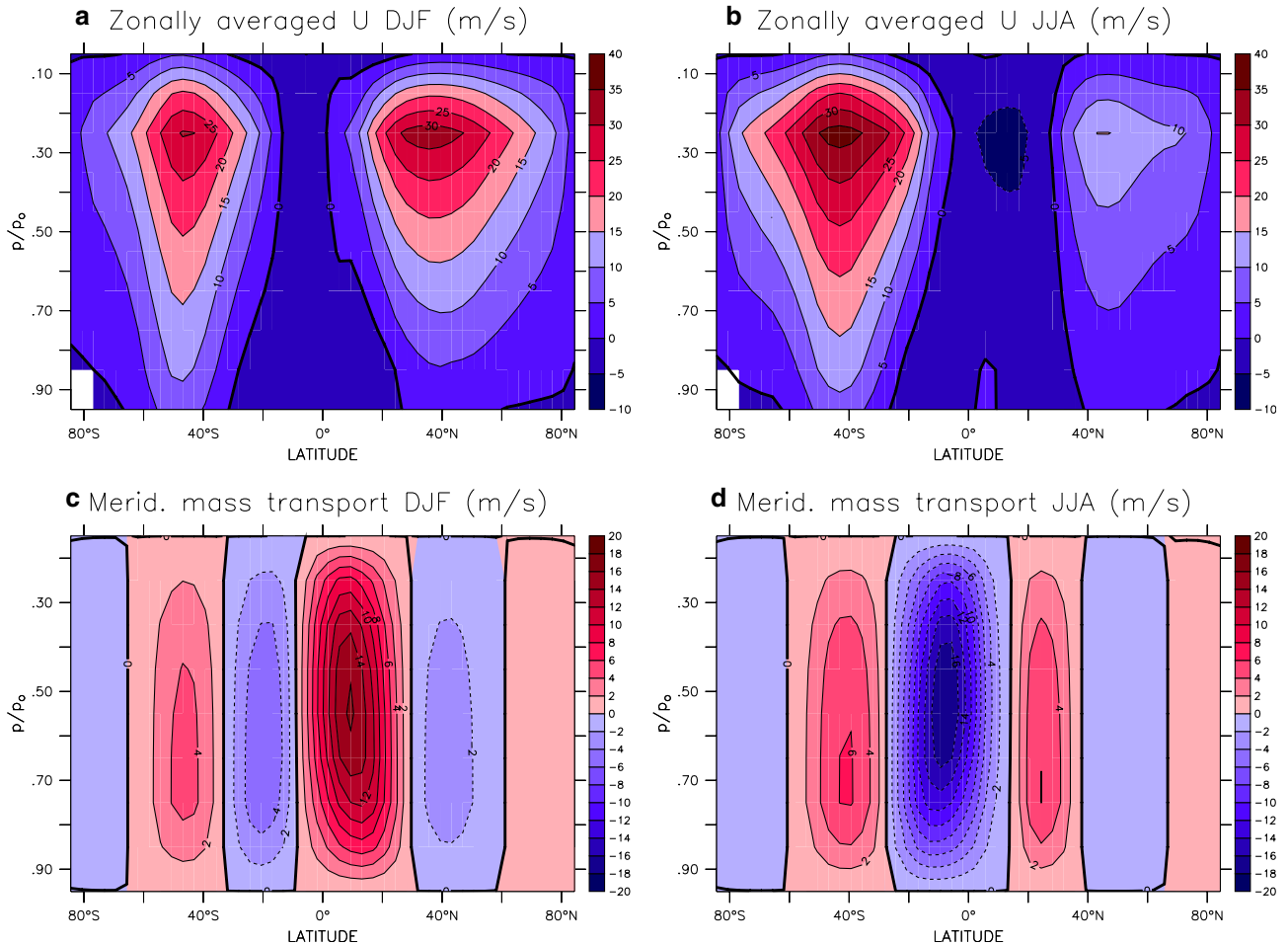
Fig. 9 Zonally averaged zonal wind component **a** in December to February and **b** in June to August (in ms^{-1}), and meridional mass transport streamfunction **c** in December to February and **d** in June to August (in 10^{10} kgs^{-1}) simulated in the control run by the model

well. The intensities of such features are only slightly underestimated relative to the observations (e.g. Peixoto and Oort (1992)). Compared to CLIMBER-2 (Petoukhov et al. 2000), CLIMBER-3α shows a slightly weaker atmospheric circulation, both in DJF and JJA, which could be related to its weaker meridional temperature gradient (not shown). The jet streams are weaker for VD04 than for VD01, especially in JJA over the Southern Hemisphere, consistent with the warmer temperatures at mid-high latitudes which further decrease the meridional temperature gradient.
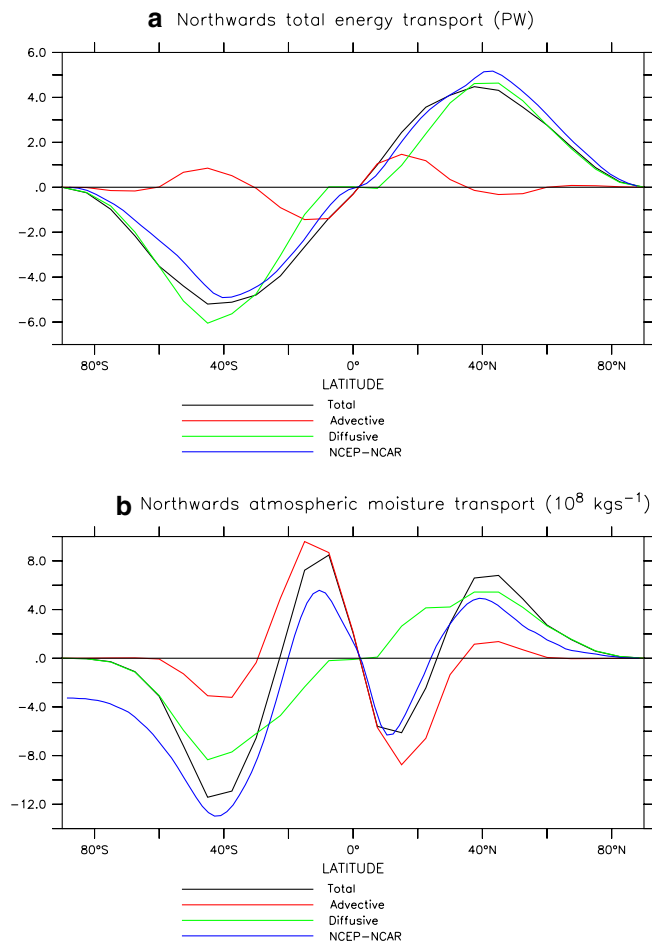
Figure 10 shows the advective, diffusive (corresponding to the transient eddy fluxes, parametrised as diffusion in the atmospheric model) and total heat and moisture transport by the atmosphere compared to those inferred from the NCEP-NCAR reanalysis (Trenberth and Caron 2000; Kistler et al. 2001). Both the total heat and moisture transport simulated by the model agree satisfactorily with the corresponding NCEP–NCAR data, thus justifying the use of the simulated winds for the advection of heat and moisture in the atmosphere, even if the the wind anomaly model is used to force the ocean as explained above (Sect. 2.3).

3.2 Atmosphere–ocean fluxes

Figure 11 compares the mean annual heat and freshwater fluxes (precipitation minus evaporation) into the ocean as simulated by CLIMBER-3α against the adjusted Southampton Oceanography Centre (SOC) surface flux dataset. The latent heat flux (for the calculation of evaporation) and net heat flux were taken from the adjusted SOC surface flux dataset (Grist and Josey 2003), while precipitation was taken from the original SOC dataset (Josey et al. 1998). The SOC database was chosen because, among several surface heat flux datasets analysed, it shows the best agreement (to within 10 Wm^{-2}) with the Woods Hole Oceanographic Institute research buoy measurements made during the Subduction Experiment in the Northeast Atlantic (Josey 2001).

The model reproduces very well the general pattern of heat gain by the ocean in the Tropics and heat loss in the subtropics, as well as the intensities of these features. The heat loss maxima around the North Atlantic, North Pacific and off the Cape of Good Hope are also captured. The model shows too much heat loss in the Irminger Sea, while the small area of heat gain located in the vicinity of

a Northwards total energy transport (PW)

b Northwards atmospheric moisture transport (10^8 kg s^{-1})

Fig. 10 Mean annual net **a** total (ocean and atmosphere) energy transport (in PW) and **b** moisture transport (in 10^8 kg s^{-1}) simulated in the control run by the model (*black* total, *red* advective, *green* diffusive) compared to estimates from the NCEP-NCAR reanalysis (*blue*). Positive values indicate transport to the north

Newfoundland in the data extends to the southern tip of Greenland in the model. Finally, the Southern Ocean is characterised by a weak heat loss in the model, although the data suggest areas of heat gain, for example, off the Weddell Sea. This discrepancy might contribute to the overestimated winter sea-ice extent in the Southern Hemisphere. Overall, the net heat flux simulated by the model agrees well with the SOC data.

The net simulated precipitation minus evaporation captures the general pattern with net precipitation over the tropics and mid and high latitudes and net evaporation in the subtropical gyres. Yet, the pattern is far from perfect. Many disagreements can be traced back to the precipitation field. For example, the precipitation maximum around the ITCZ is too broad, and the maxima structures over the Indian and Pacific Oceans are not captured properly. The errors reflect likely both the deficiencies in moisture transport and in the simulation of the processes related to precipitation.

Although we have not carried out a detailed sensitivity study to analyse this matter further, it is clear that

the coarse resolution will not allow capturing many regional details of the fields. Hence, it is very likely that the coarse zonal resolution could explain many of the deficiencies shown by the surface fluxes as explained in Sect. 2.1.

3.3 Oceanic fields

3.3.1 Tracer distribution

In the following, the oceanic tracer fields as obtained for the standard configuration of the model are described. Most of the plots shown correspond to VD01, with background diapycnal diffusivity $\kappa_v^{bg} = 0.1 \times 10^{-4}$ m^2 s^{-1}. These oceanic fields are in general very similar to the ones with a background diapycnal diffusivity of $\kappa_v^{bg} = 0.4 \times 10^{-4}$ m^2 s^{-1} in VD04. Significant differences are pointed out in the text.

The annual mean simulated SST averaged over the last 10 years of the control run and its anomalies relative to the Levitus (1982) climatology are shown in Fig. 12a, b. The major features in the SST fields are reproduced, including the strong gradients associated with the major currents such as the North Atlantic, Kuroshio and Antarctic Circumpolar Current (ACC). Owing to the coarse resolution of the model, these currents are, however, broader and slower (Sect. 3.3.2) and the modelled tracer gradients are not as sharp as in the observations. This leads to substantial regional temperature differences between the model and the observations. In addition, the structures are too zonal in the mid-latitudes, and the SST tends to be warmer than observed in the low latitudes. These maxima are weakened with increased diapycnal mixing. Along the western coasts of North and South America and Africa, the surface water masses are found to be too warm, indicating too weak equatorial upwelling and too weak eastern boundary currents in these areas. The surface waters around Antarctica are slightly too cold. This discrepancy is reduced with an increased diapycnal mixing κ_v, but the front in the ACC is broadened. In general the maximum deviations relative to Levitus (1982) are of about 7°C (not shown), which is of the same magnitude as those from the HADCM-2 model without flux adjustment (Gregory and Mitchell (1997); see also the discussion in Houghton et al. (2001)).

The annual mean simulated sea surface salinity (SSS) averaged over the last 10 years of the control run is shown in Fig. 12c, together with its anomalies relative to the Levitus (1982) climatology (Fig. 12d). As in the observations, the SSS is maximum in the subtropics in the model, essentially due to the excess of evaporation over precipitation. The zonal extension and strength of the maxima in the Pacific are slightly too large. In the Atlantic the subtropical maximum is also slightly too strong in the north, but too weak in the south. The main discrepancies between the model and the observations
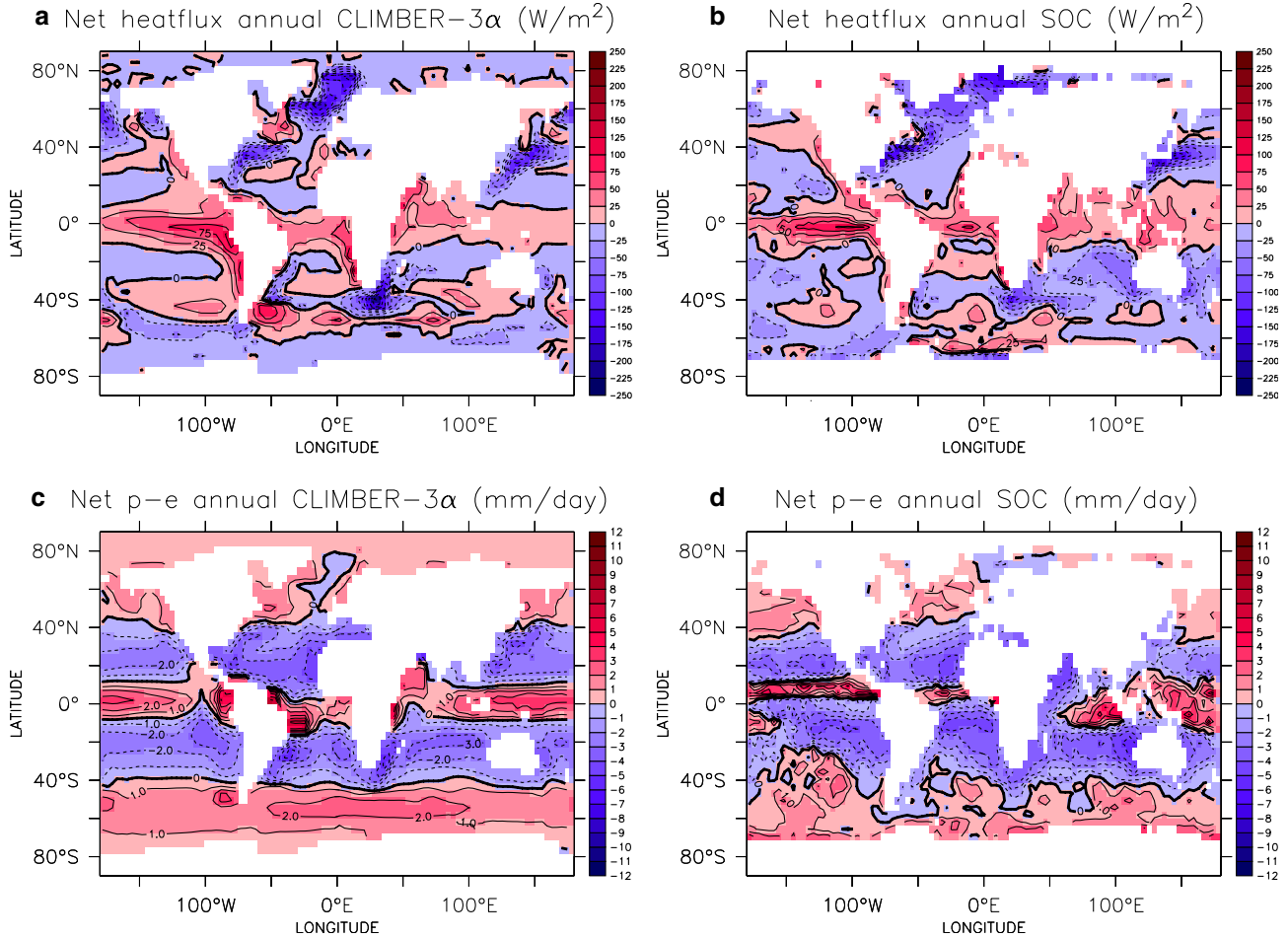
Fig. 11 Mean annual net heat (**a**, **b** in Wm^{-2}) and freshwater (precipitation minus evaporation) fluxes (**c**, **d** in mm/day) simulated in the control run by the model and given by the SOC-adjusted database, respectively. Positive fluxes are into the ocean

are along the north-eastern coast of Brazil and in the Arabian Sea because of anomalously strong precipitation in these regions (Sect. 3.2), in the North Pacific, which is too salty, consistent with too little precipitation in the storm-track area (Fig. 5) and possibly an anomalous Pacific overturning circulation (Fig. 19), which might lead to enhanced salt transport to the north at the surface, and in the North Atlantic around 50°N. The atmospheric freshwater flux as well as fresh water from ice melting is quite realistic in this area, and is thus not the origin for this discrepancy. It rather results from the anomalously broad East Greenland Current that imports fresh water from the Arctic into the North Atlantic (see Sect. 3.3.2). This is a consequence of the low resolution. In reality, most of the fresh water does not leave the GIN Seas, but circulates back partly in the Jan Mayen current and partly in a thin boundary current around Greenland and into the Labrador Sea. The extent and magnitude of this freshwater tongue decreases with higher background diapycnal diffusivity κ_v. It is even further decreased when using the FCT tracer-advection-scheme, which introduces strong spurious mixing (Boris and Book 1973; Gerdes et al.1991) (see Part II of this paper). However, as mentioned in Sect.

2.4, it should be kept in mind that κ_v represents the mixing in the ocean interior, away from oceanic boundaries. Most of the wind-induced mixing at the ocean surface is already captured by the KPP parametrisation. Improving surface tracer distributions through a higher interior mixing coefficient should therefore be interpreted with care, since problems with the inaccurate representation of the oceanic transport or surface forcing might be artificially corrected through mixing in the ocean interior and therefore might be just masked.

The representation of deep water masses in the Atlantic can be inferred from Fig. 13, where temperature and salinity sections at 28°W are compared to the Levitus (1982) climatology. The general features are well reproduced. The imprints of NADW, Antarctic Intermediate Water (AAIW) and Antarctic Bottom Water (AABW) are readily apparent in the salinity distribution. Note that NADW almost reaches the surface in the Southern Ocean. The temperature section shows the typical w-shape structure imposed by the subtropical Ekman cells. The Atlantic is slightly too stratified compared to the observations, i.e., the intermediate to deep water masses are too cold and salty. NADW, characterised by a salinity of approximately 34.9 psu
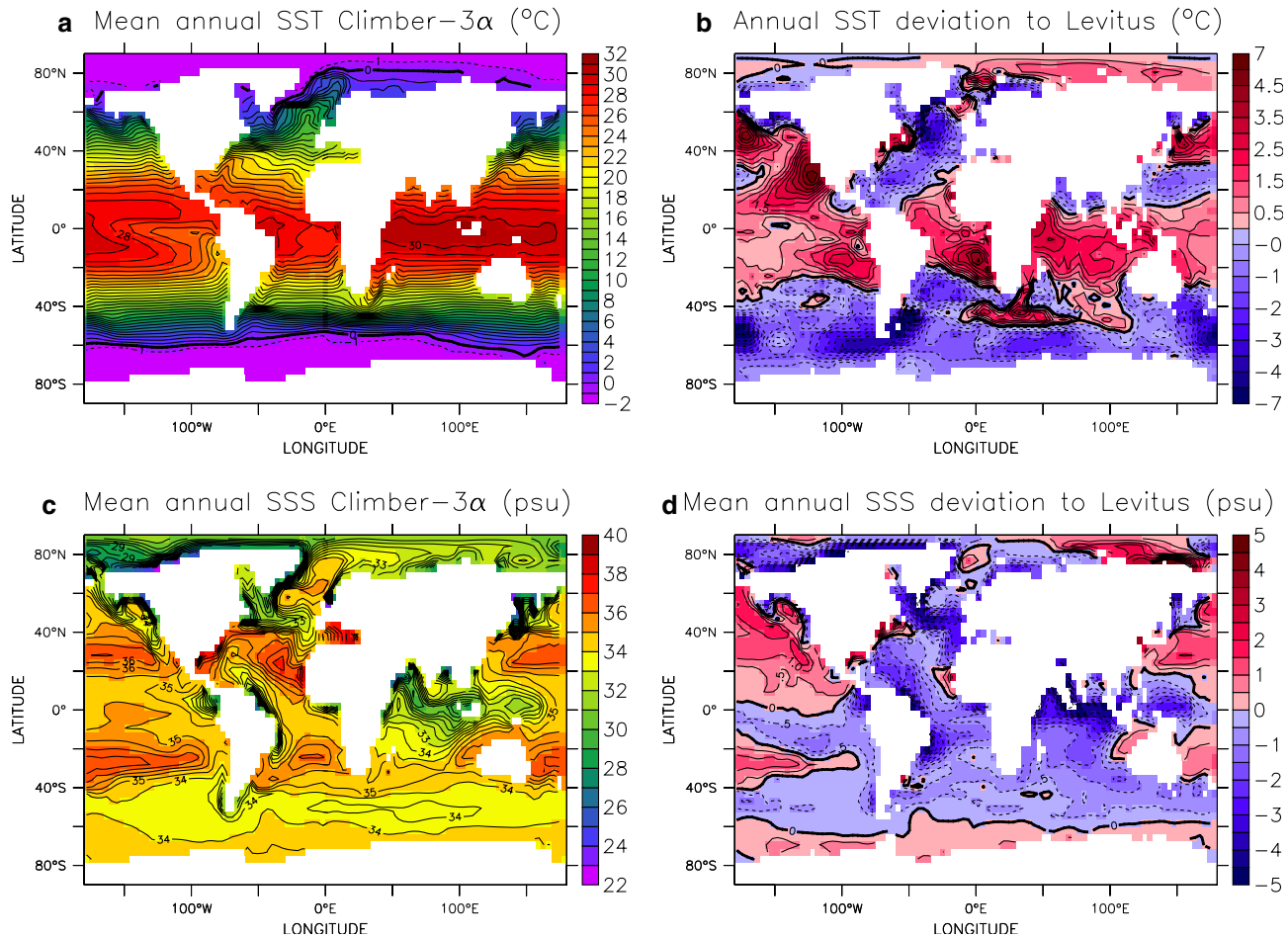
Fig. 12 Mean annual sea-surface temperature (*SST*) (**a** in °C) and sea-surface salinity (**c** in psu) simulated in the control run by the model and their deviations relative to the Levitus dataset (**b**, **c**)

and a temperature between 2°C and 4°C, is formed in the Nordic seas of the North Atlantic, sinks to the bottom and flows southward. It is easily seen in the model, although it only reaches about 3000 m in depth. AABW ($T \simeq -0.5$°C, $S \simeq 34.7$ psu), formed in the Southern Ocean and invading the bottom of the basin, is slightly too cold and too saline in the model. Note that the penetration of fresh AAIW below the thermocline at 50°S is very well reproduced. The Pacific also appears too stratified in temperature compared to the observations (Fig. 14a, b), with warmer surface waters and colder bottom waters. The depth of the thermocline is, however, consistent with the observations. The upper Pacific basin is also too salty, especially in the Northern Hemisphere (see discussion above) where the penetration of fresh waters beneath the halocline at 50°N is not reproduced in the model (Fig. 14c, d).

In both basins, increasing the diapycnal diffusivity leads to a decrease in stratification at depth. Temperatures below 2,000 m are closer to observations for VD04 as can be seen for the Atlantic in Fig. 15. The same holds for salinities at depth. However, the upper ocean tracer distribution both in the Atlantic and the Indo-pacific are not as well represented with higher diapycnal

background diffusivity. The AAIW imprint is substantially worsened, and there is much less upwelling of NADW in the Southern Ocean in contrast to the picture apparent from the Levitus salinity distribution.

Figure 16 shows the $\Delta^{14}C$ distribution simulated by the model in the control run both for VD01 and VD04 compared to WOCE data (Schlitzer 2000; Key et al. 2004). The overall pattern of $\Delta^{14}C$ distribution in VD04 is closer to WOCE data than in VD01, although the deep Atlantic and, especially, the deep Pacific water masses are still too old compared to observations. In VD01 these waters are not only much too old but AABW is not ventilated enough, leading to an unrealistic low $\Delta^{14}C$ signal. In both cases the pronounced $\Delta^{14}C$ signal with values between $-50\%_0$ to $-130\%_0$ penetrating from the sea surface into the deep North Atlantic compares well to the observations.

3.3.2 Ocean circulation

Figure 17 shows the surface horizontal circulation in CLIMBER-3α. The major current structures are realistically simulated (e.g. Stammer et al. 2002). The western boundary currents are too broad and too
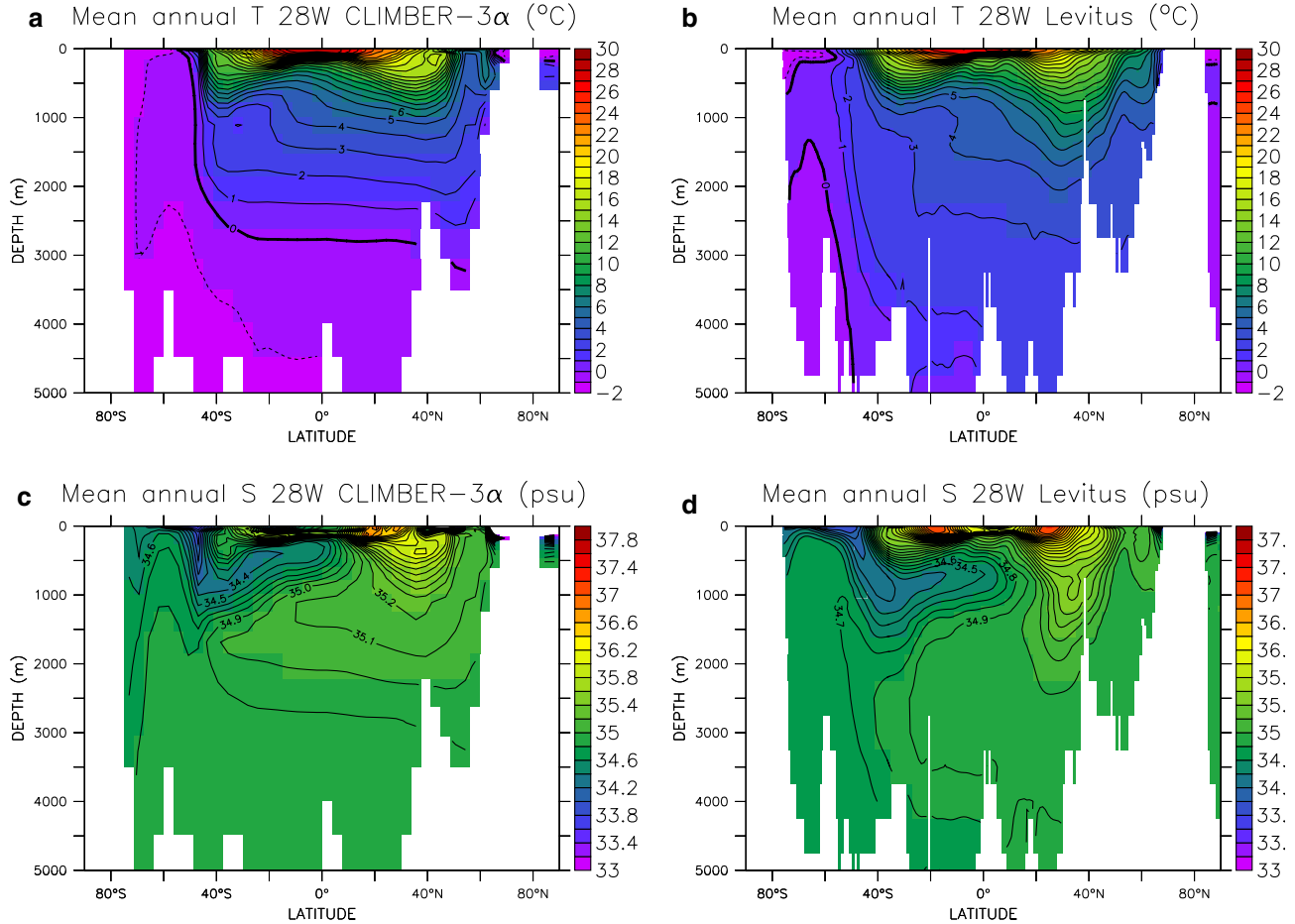
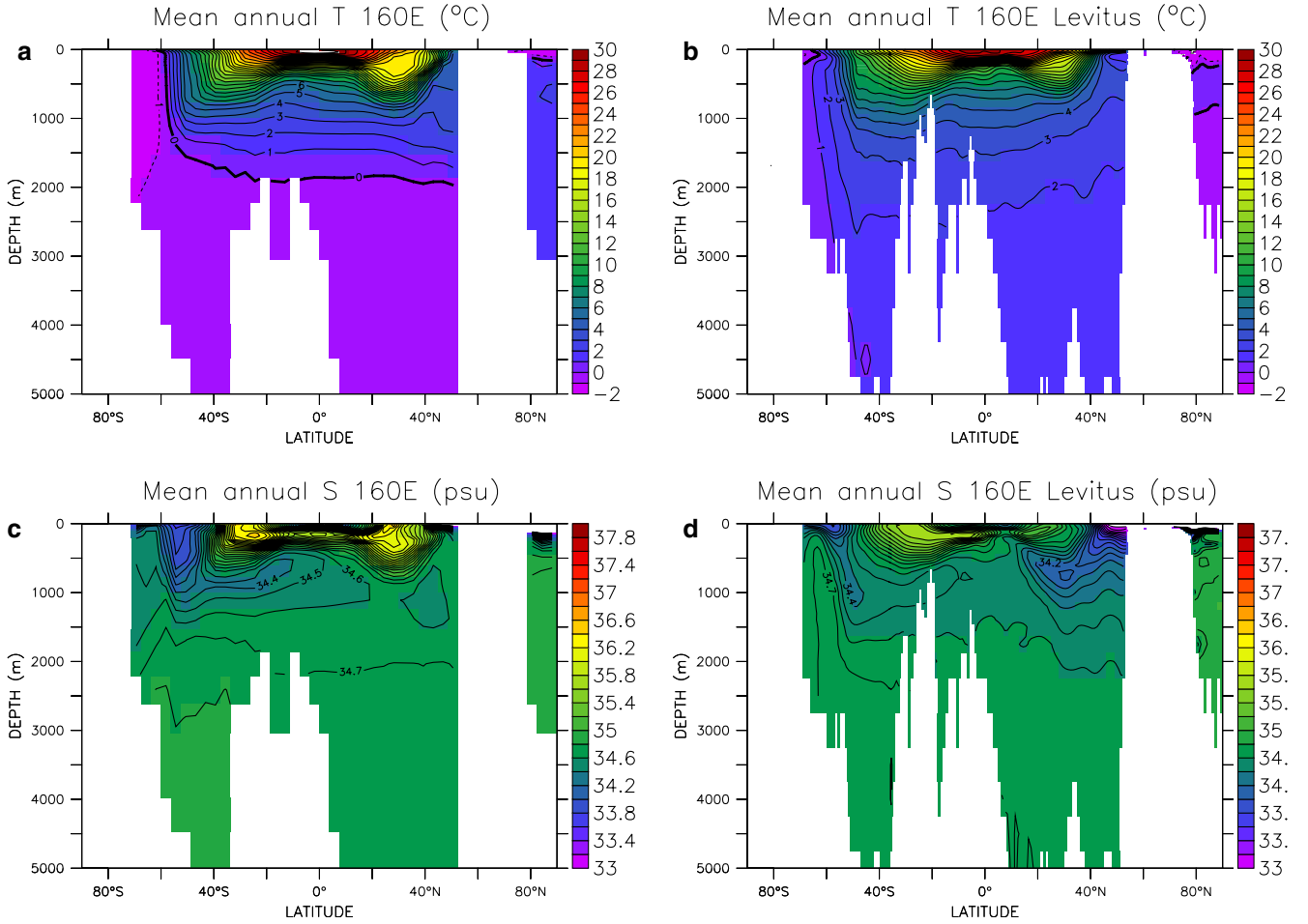**Fig. 13** Temperature (**a**, **b** in °C) and salinity (**c**, **d** in psu) profile along 28°W simulated in the control run by the model and in Levitus, respectively

zonal, which is a common deficiency of coarse resolution models. In high North Atlantic latitudes, this coarse resolution does not allow the North Atlantic Current to partly enter the Barents Sea and the whole flow thus heads west of Spitsbergen. Note that the Labrador Sea spans only two velocity grid points and is thus too narrow to allow a proper representation of the circulation in this area. The East Greenland Current thus entirely recirculates eastward at the southern tip of Greenland, instead of partly entering the Labrador Sea along the West Greenland Current. The net southward transport across the Denmark Strait is about 6.1 Sv (3.2 Sv northward, 9.3 Sv southward), which is about twice as large as the value of 3.3 Sv which is inferred from observations by Hansen and Østerhus (2000). This deficiency is directly linked to the coarse resolution, as the Denmark Strait had to be artificially broadened to allow a proper representation of the East Greenland Current. As noted above, this deficiency is primarily responsible for the excess of fresh water in the northern North Atlantic. The simulated net transport across the Iceland–Scotland ridge is with 5.3 Sv (10.3 Sv northward, 5.0 Sv southward) slightly larger than the observational estimate by Hansen and Østerhus (2000) of 4.0 Sv.

In the barotropic streamfunction of the vertically integrated velocities of Fig. 18, one can see the horizontal volume transport (in Sv) that is associated with these currents. The strength of the subtropical gyres in the North Atlantic and North Pacific of 27 Sv and 39 Sv, respectively, are consistent with observational estimates given, for example, by Schott et al. (1988) and by Hautala et al. (1994). The strength of the ACC is indicated by a mean mass transport of 57 Sv (61 Sv for VD04) through the Drake Passage, while Lambert and Boer (2001) found an average of 92 Sv for a number of coupled models and observational estimates are of the order of 135 Sv (Nowlin and Klinck 1986). Since the ACC is a current determined by the density gradients extending all the way from top to bottom, the too weak ACC can partly be attributed to too weak density gradients in the Southern Ocean below 1,500 m.

Figure 19 shows the zonally averaged meridional streamfunctions of the present-day equilibrium simulations for different oceanic basins in VD01. The Atlantic overturning in the upper panel of the figure has a maximum strength of about 12 Sv. Even though this value is rather weak, it is not inconsistent with observational estimates (Ganachaud and Wunsch 2000; Talley et al. 2003). A stronger overturning with a northern cell

Fig. 14 Temperature (**a**, **b** in °C) and salinity (**c**, **d** in psu) profile along 160°E simulated in the control run by the model and in Levitus, respectively

deepened to about 3,000 m (Fig. 20) is obtained by increasing the diapycnal diffusion coefficient κ_v. Note that in VD04 there is a substantial amount of upwelling of deep water masses up to the surface in the Indopacific (Fig. 20, middle and lower panels) which is not the case for lower diapycnal diffusivity of VD01 (Fig. 19). On the other hand, upwelling of NADW in the Southern Ocean is substantially reduced for higher κ_v which has a negative effect on the salinity distribution of the Southern Ocean (not shown). In this case, most NADW upwells in the Indopacific after having been mixed with other water masses. Whether, in reality, there is a substantial amount of deep upwelling to the surface is still unresolved; however, it has been strongly argued that most NADW upwells in the Southern Ocean and that there is no deep upwelling in the Indopacific (Toggweiler and Samuels 1993; Gnanadesikan and Toggweiler 1999; Wunsch et al. 1983; Robbins and Toole 1997).

The deep water masses form mainly in the GIN and Irminger Seas, as can be seen from the mixed layer depth in Fig. 21. Deep convection has been observed in the GIN Sea, e.g., by Marshall and Schott (1999), while only recent measurements suggest convection in the Irminger Sea (e.g. Bacon et al. 2003). Note that as opposed to

observations (e.g. Lab Sea Group (1998)), the model does not show deep convection in Labrador Sea. This is again due to the narrowness of this area in our coarse resolution points.
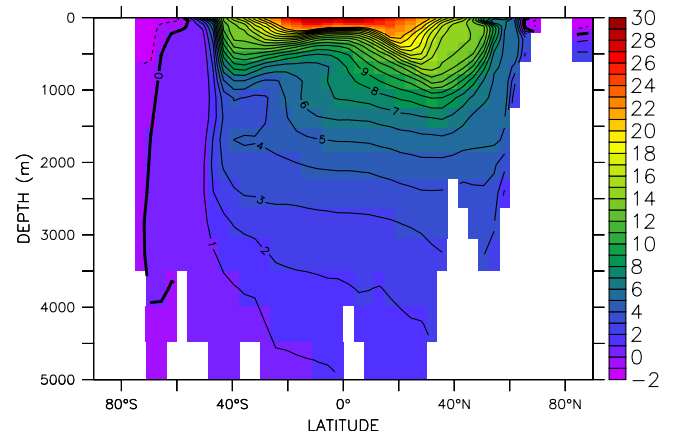
Fig. 15 Temperature (in °C) profile along 28°W simulated in the control run with increased background diapycnal diffusivity of $\kappa_v^{bg} = 0.4 \times 10^{-4}$ m^2 s^{-1}
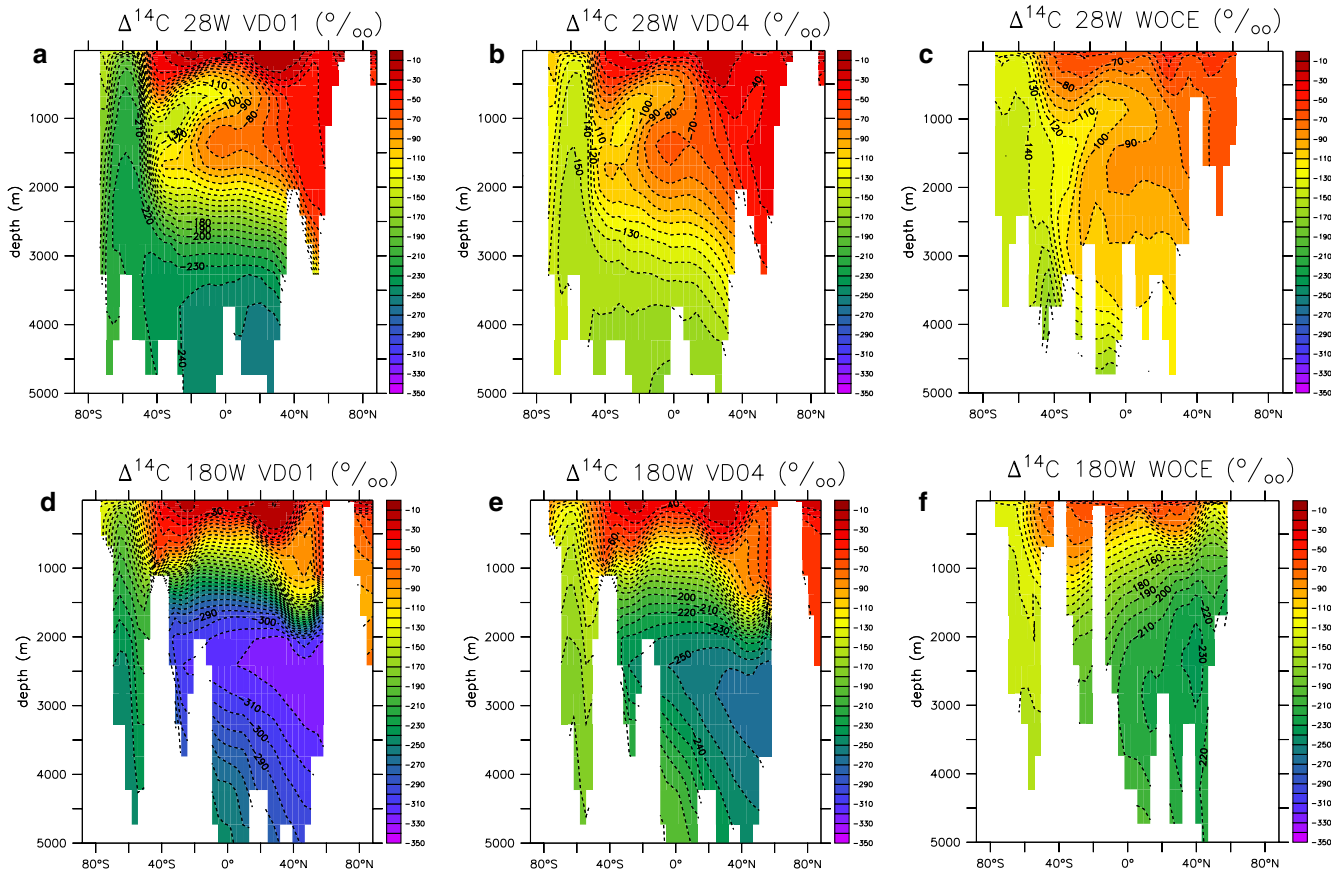
Fig. 16 Δ^{14}C concentration across a section at 28°W in the Atlantic Ocean simulated by the model **a** in VD01, **b** in VD04, and **c** from WOCE data, and across a section at 28°W in the Pacific Ocean simulated by the model **d** in VD01, **e** in VD04, and **f** from WOCE data (in ‰)

The outflow of NADW into the Southern Ocean at 35°S, corresponding to the maximum value of the Atlantic overturning streamfunction at that latitude, is about 7 Sv in VD01 and increases slightly to about 8 Sv in VD04. The streamfunction of the Indo-Pacific basin (Fig. 19, middle panel) consists mainly of the Ekman cells in the upper layers and a small overturning cell in the Northern Hemisphere which is not seen in observations. This is due to anomalously saline upper water masses in the North Pacific between 40°N and 60°N and leads to a slightly stronger northern overturning maximum in the global streamfunction (Fig. 19, bottom panel) compared to the Atlantic.

AABW is mainly formed in the Weddell and the Ross Sea (Fig. 21). Note that very little deep convection occurs in the open Southern Ocean, consistent with observations. The global AABW reaches a maximum of 14 Sv of which 11 Sv enter the Indo-Pacific and 3 Sv flow into the Atlantic basin. Southern Ocean winds lead to an upwelling of about 24 Sv around 60°S of which 10 Sv directly downwell between 30°S and 50°S forming the so-called Deacon cell in the global streamfunction (Döös and Webb 1994; Speer et al. 2000). The values increase slightly for VD04.

Finally, meridional oceanic heat and freshwater transports for the Atlantic and global oceans are shown

in Fig. 22. The model's Atlantic meridional heat transport agrees reasonably well with empirical estimates in the Southern Atlantic but there are large discrepancies in the North Atlantic, where the model's oceanic heat transport is about 50% weaker than the data. This results from the relatively weak overturning circulation in the model and is a common deficiency of coarse OGCMs. The effect is due to the broad and slow boundary currents (e.g. Kamenkovich et al. (2000)) and possibly to a recirculation of deep waters within the Atlantic basin primarily along the boundaries, resulting in a reduced efficiency of the overturning (Mignot et al., unpublished data). The poleward heat transport at 25°N is about 0.68 PW, and the strength of the NADW cell at this latitude is 9 Sv. These values are in good agreement with the linear relation found by Böning et al. (1996) from a variety of models with different resolutions and forcings:

$$\text{(Heat transport at 25°N)} = 0.2 + 0.05 \times \text{(NADW at 25°N).} \quad (3)$$

The main characteristics of the global oceanic heat transport are consistent with observations (Fig. 22a, c). The maximum implied ocean heat transport in northern mid-latitudes is too weak because of the too weak

Fig. 17 Surface ocean currents (at a depth of 12.5 m) simulated in the control run by the model, in cm s^{-1}
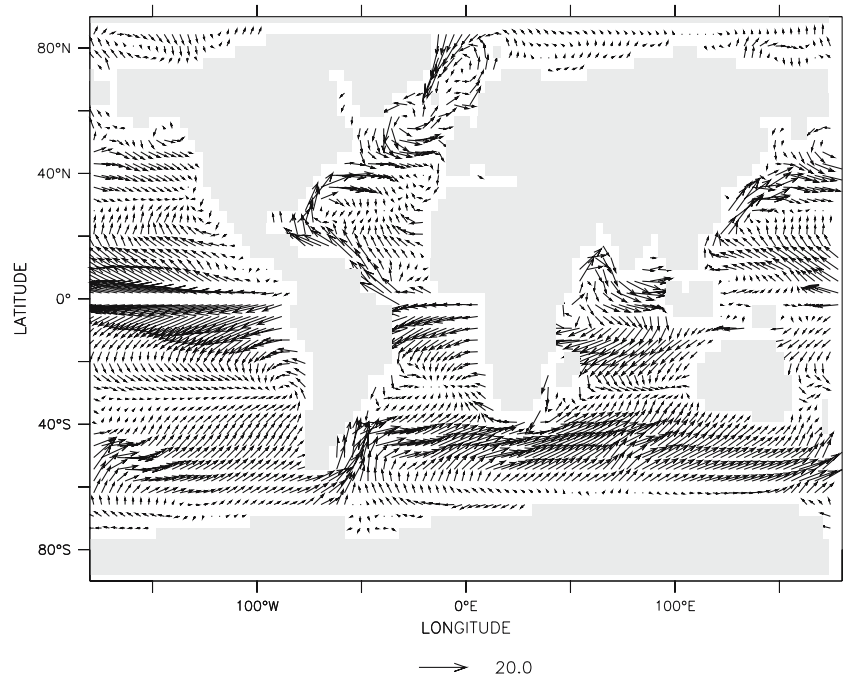
Fig. 18 Vertically integrated barotropic streamfunction (in Sv) derived from the zonal velocity field. Spacing in the contour lines is 10 Sv. The subtropical gyres in the North Atlantic and North Pacific have a strength of 27 Sv and 39 Sv, respectively. The ACC strength of 57 Sv is weak compared to observations
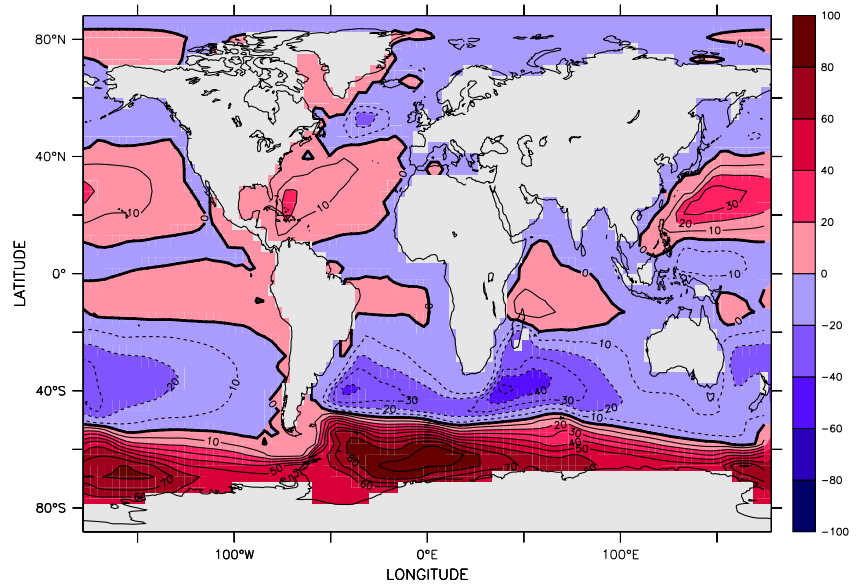
transport in the Atlantic as commented above. It increases slightly for VD04 higher background diffusivity as a consequence of the stronger meridional circulation. The global oceanic heat transport is consistent with the observations, suggesting that the Indian and Pacific oceanic heat transports are slightly overestimated in the model.

The Atlantic and global implied oceanic freshwater transports are represented in Fig. 22 (panels b, d) together with direct estimations derived from oceanic sections in the Atlantic. The Atlantic northward freshwater transport decreases in VD04. It is slightly underestimated in the north and south Atlantic mid-latitudes but lies within the error bars. Data are more sparse in the Tropics and the modelled transport seems to be too strongly northward. The global northwards oceanic freshwater transport is slightly weaker in VD01 than in VD04.

3.4 Sea-ice fields

The 10-year-averaged sea-ice concentration in the control run for VD01 is shown in Fig. 23 for different

Fig. 19 Zonally averaged streamfunction for different basins for VD01 (vertical background diffusivity $\kappa_v^{bg} = 0.1 \times 10^{-4}$ m^2 s^{-1}). Atlantic basin (*upper panel*), Indo-Pacific basin (*middle panel*) and global (*lower panel*)
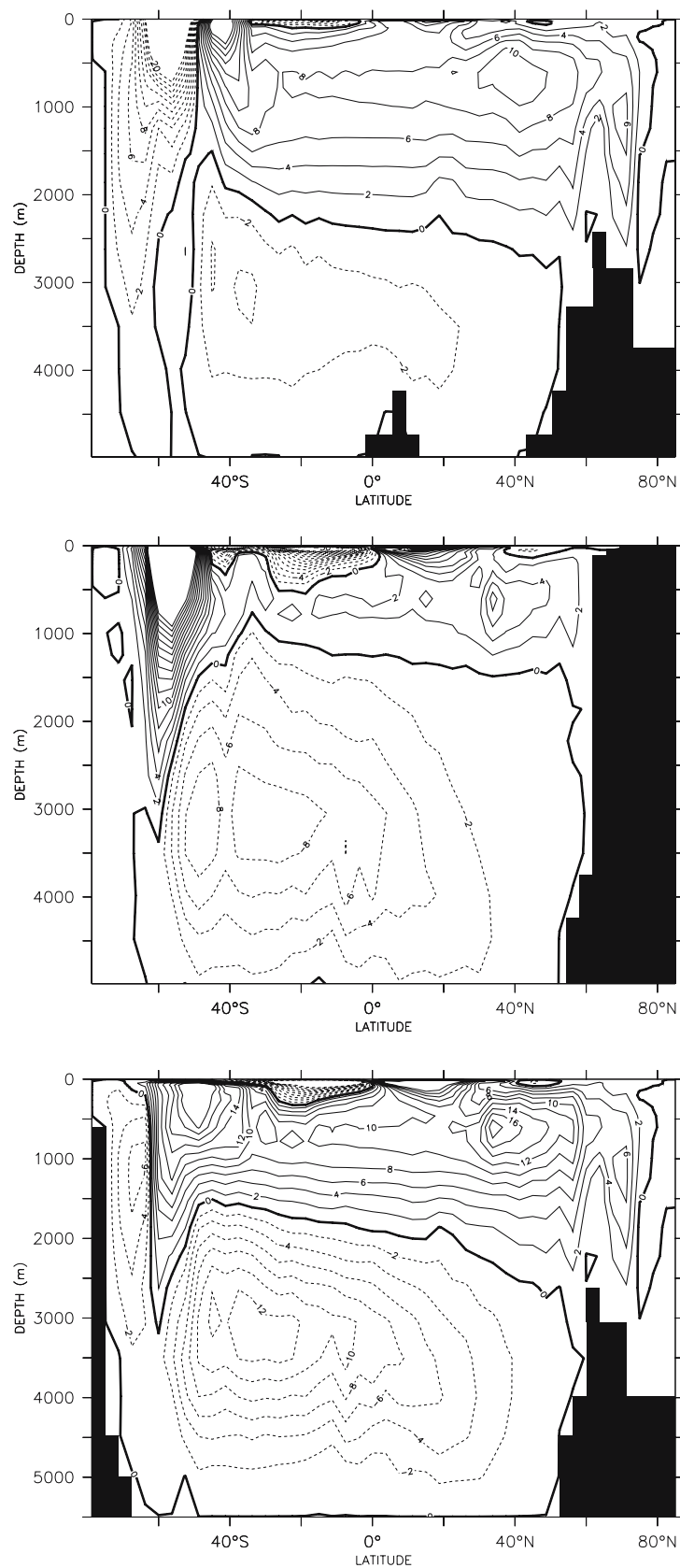
Fig. 20 Zonally averaged streamfunction for different basins for VD04 (vertical background diffusivity $\kappa_v^{bg} = 0.4 \times 10^{-4}$ m^2 s^{-1}). Atlantic basin (*upper panel*), Indo-Pacific basin (*middle panel*) and global (*lower panel*)
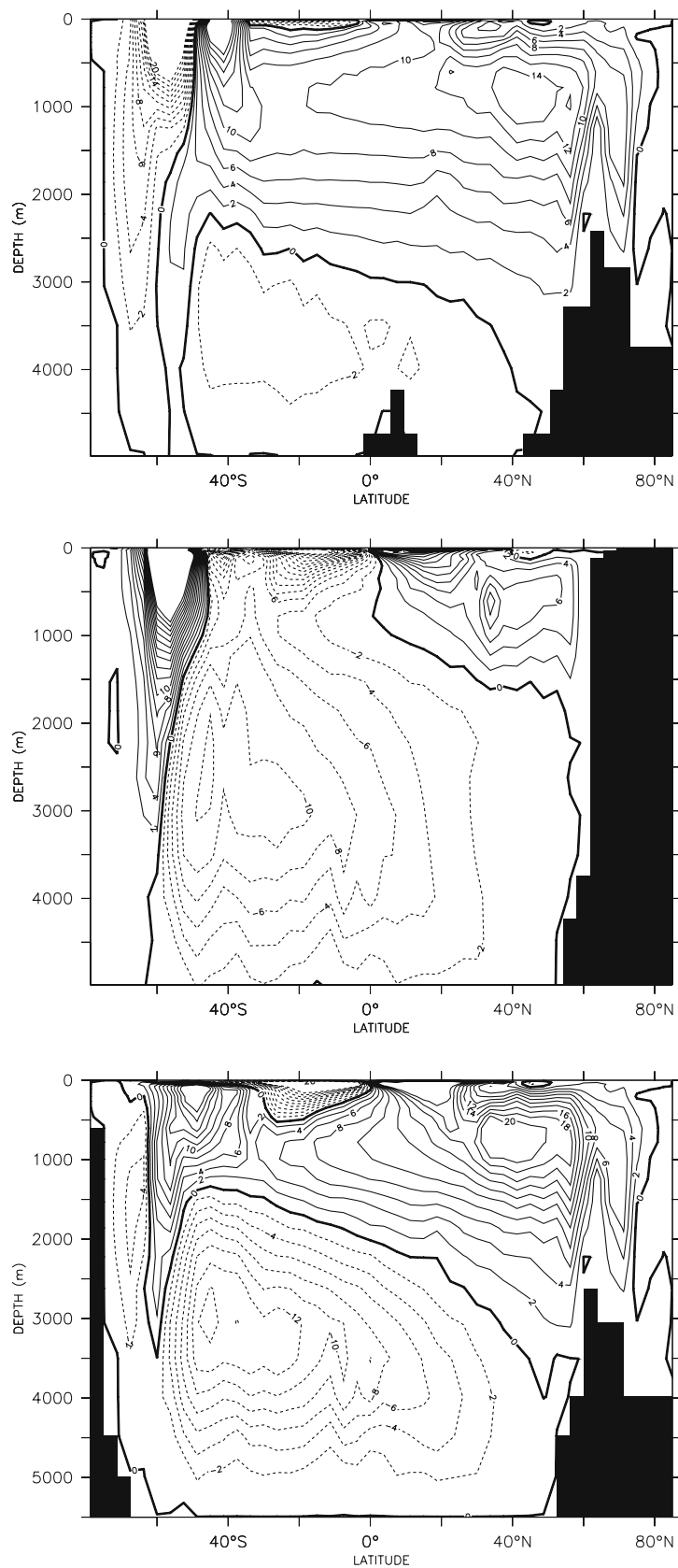
Fig. 21 Maximum mixed layer depth in the control run (in m). The mixed layer was calculated at each point as the depth at which the potential density within the underlying water column exceeds that of the surface by 0.125 kg m^{-3}. Deep convection occurs in the GIN and Irminger Seas in the North Atlantic and in the Weddell and Ross Seas in the Southern Ocean
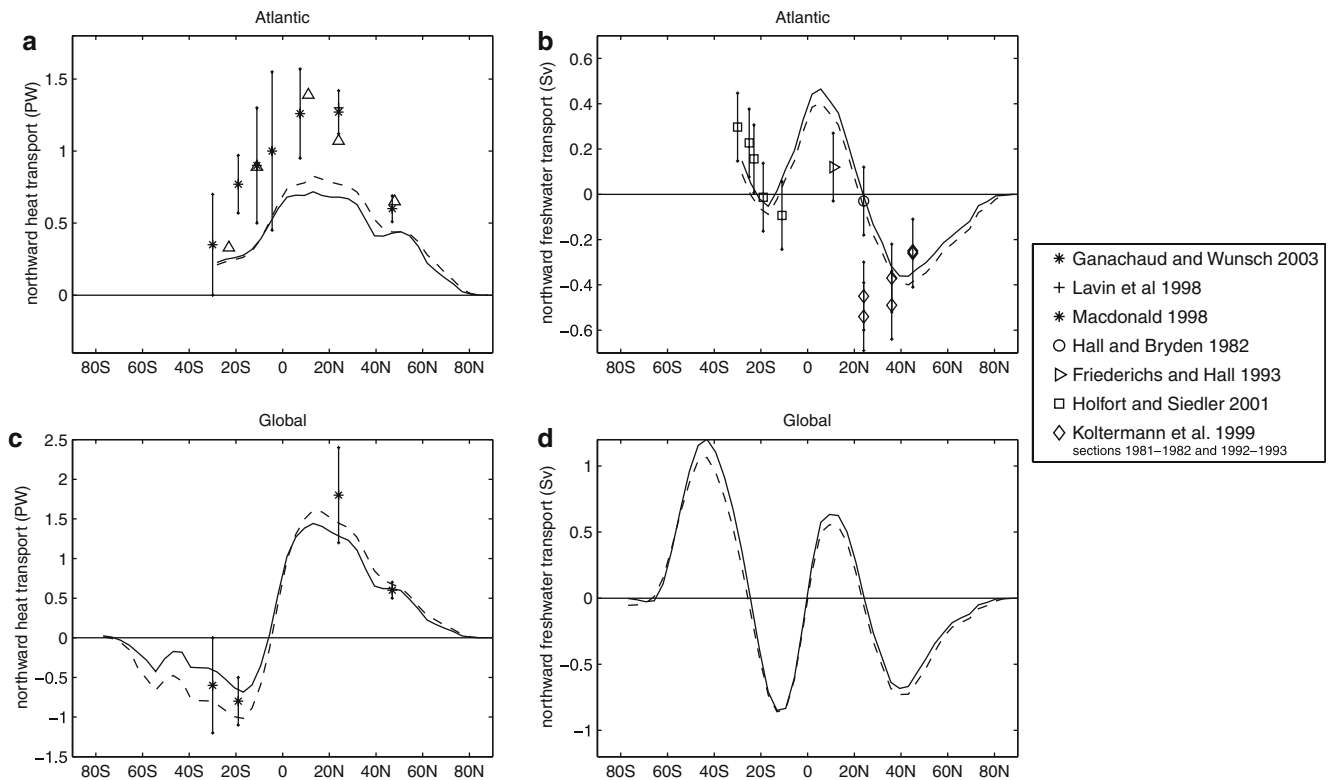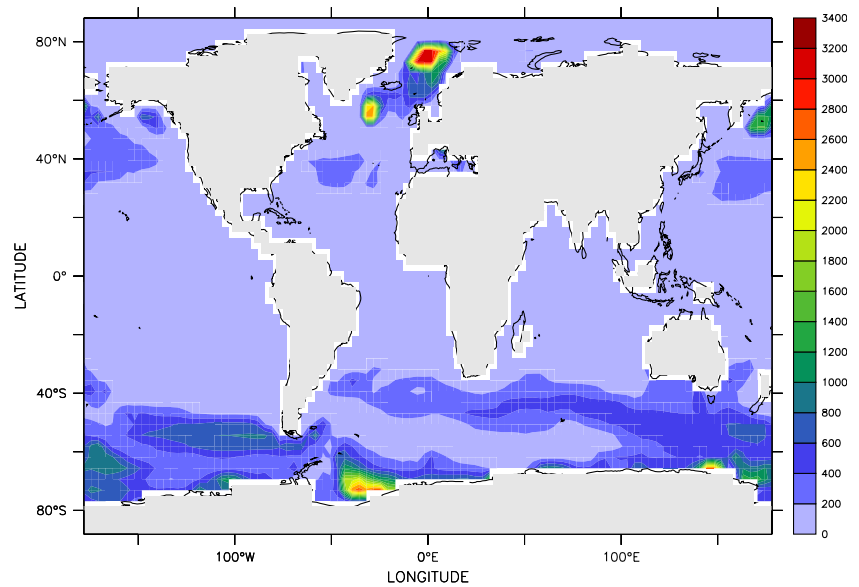
**Fig. 22** Northward implied ocean heat transport (PW) for the Atlantic (**a**) and for the global (**c**) ocean. **b**, **d** Same for the freshwater transport (Sv) relative to the freshwater transport through Bering Strait (*solid line* VD01, *dashed line* VD04). *Symbols* show a selection of recent hydrographic estimates of the heat transport (**a** and **c**) and direct freshwater transports estimates derived from ocean sections (**b** and **d**). *Error bars* for the freshwater estimates are 0.15 Sv after Wijffels ([2001])

seasons. The main features of simulated Arctic March sea-ice extent are well reproduced compared to observations (Parkinson et al. [1999]). Its total annual area extent of 8.3×10^6 km^2 is within the observed variability around estimates of 13×10^6 km^2 inferred from satellite data (Gloersen et al. [1992]). However, in winter, too

much ice is formed in the Labrador Sea and south of Greenland, as well as in the Barents Sea. This results from the coarse representation of the oceanic circulation in these regions. In particular, as described in Sect. [3.3.2], the warm North Atlantic current does not reach the Barents Sea and the currents south of Greenland and in
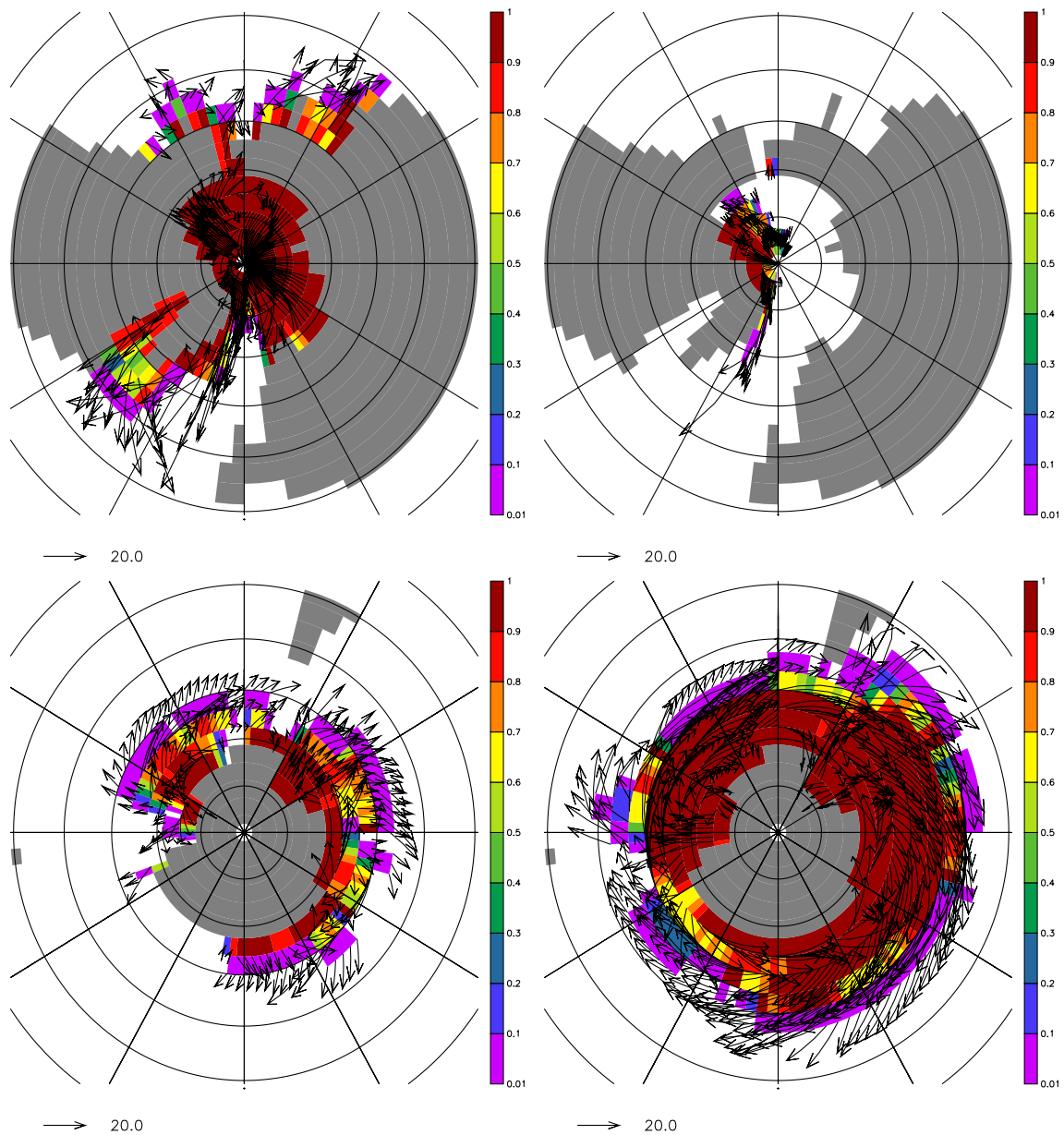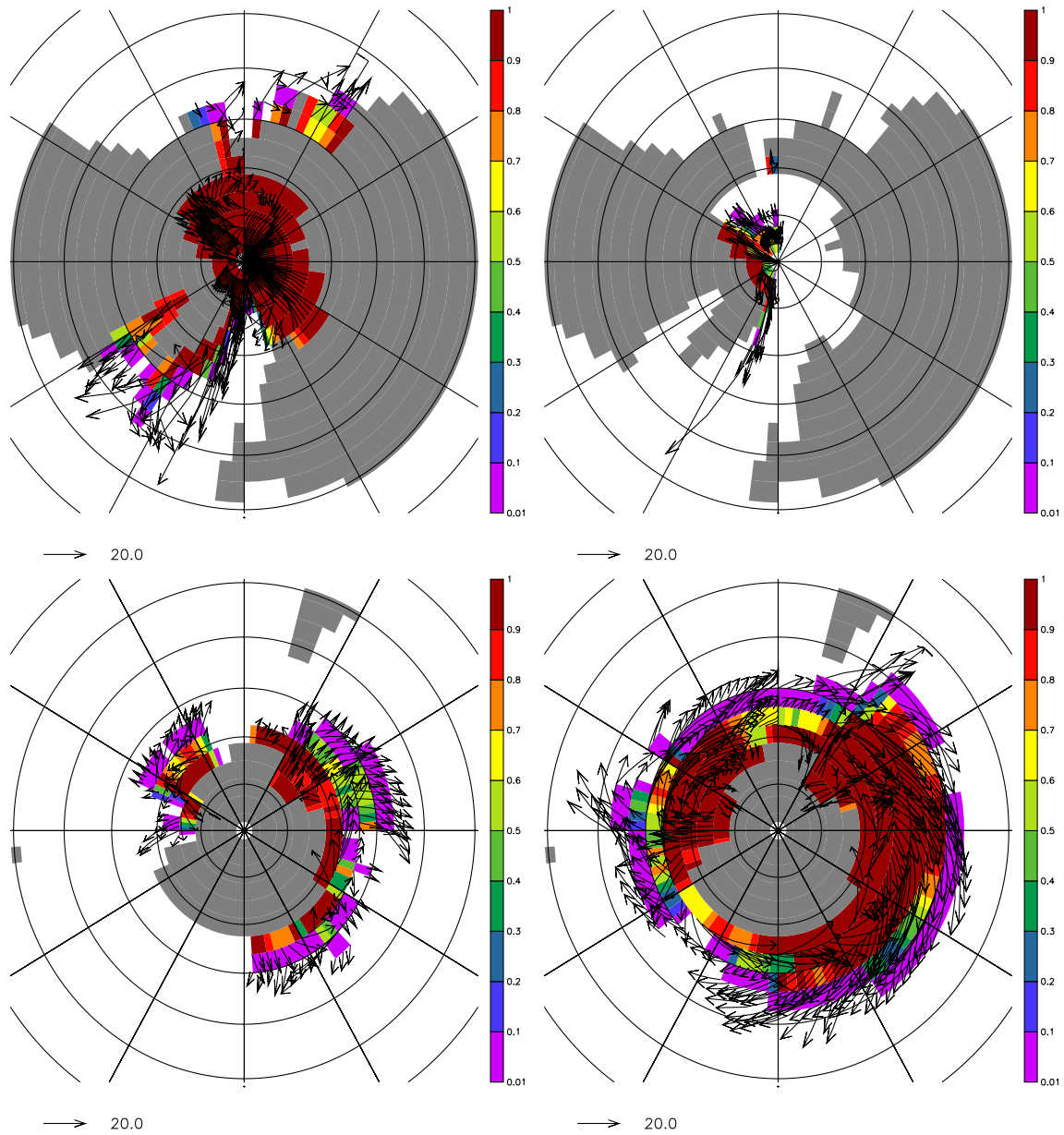
Fig. 23 Sea ice concentration in March (*left*) and September (*right*) for the polar regions in VD01. Sea ice velocities are shown as overlying vectors (in cm s^{-1})

the Labrador Sea are not properly resolved. This leads to anomalously cold waters along the coast in this area and too extensive sea-ice in the region. In summer, Arctic ice extent is generally too small as it is restricted to the Canadian basin and north of Greenland (compare the left panel of Fig. 23 for sea-ice concentration of September.) The dominant feature Arctic sea-ice advection is the transpolar drift stream. It is reproduced in the model and feeds the East Greenland Drift Stream, which is very strong and might also contribute to the slightly too large extent of sea-ice in the winter northern Atlantic. The anticyclonic gyre in the Beaufort Sea is reproduced. Overall, the latter fields improve somewhat for VD04, especially in March, where sea-ice extension

decreases in the Labrador Sea and South of Greenland and, most notably, in the North Pacific in the Sea of Okhotsk (Fig. 24).

Around Antarctica sea-ice extent in September is reproduced realistically with a slight overestimation in the South Atlantic especially in Drake Passage (see satellite data in Gloersen et al. (1992)). In March we find the same overestimation in the South Atlantic and in the Eastern Pacific sector around 120°E. The northernmost extent of sea-ice in summer in the observations is at the western border of the Weddell Sea, while it is in the Atlantic in our model. This overestimation of Antarctic sea-ice extent leads to overestimated salinities in the Southern Ocean (Fig. 12 panels c, d)) in spite of a net

Fig. 24 Sea ice concentration in March (*left*) and September (*right*) for the polar regions in VD04. Sea ice velocities are shown as overlying vectors (in cm s^{-1})

freshwater input into the ocean (Fig. 11 panels c, d). Again, the sea-ice performance is slightly better for VD04, which shows a reduction in sea-ice extension relative to VD01 both in March and September (Fig. 24). The simulation correctly shows westward motion around the Antarctic coast and eastward recirculation offshore leaving Weddell Sea and Ross Sea (Emery et al. 1997). The annual mean sea-ice extent in the Southern Hemisphere of 21.9×10^6 km^2 compares to about 11.5×10^6 km^2 from satellite observations (Gloersen et al. 1992). For higher diapycnal diffusivity of $\kappa_v = 0.4 \times 10^{-4}$ m^2 s^{-1} in VD04 sea-ice extent, generally, is reduced in both hemispheres and both in winter and summer, with annual mean values of 7.3×10^6 km^2 and 14.9×10^6 km^2 for the Arctic and Antarctic, respectively.

Sea-ice advection velocities in both hemispheres exceed estimates based on satellite measurements by a factor of two (Emery et al. 1997). The cause for the overestimated sea-ice drift is likely the fact that the sea-ice (not shown) is too thin all year round. While sea-ice draft data indicate thicknesses over 3 m over a considerable part of the Arctic (Bourke and Garrett 1987), the simulated thicknesses are below 3 m almost everywhere. Notably, the maximum thicknesses above 4 m north of Greenland and the Canadian archipelago are underestimated by 1 m. Accordingly, the annual cycle of sea ice suggests that the onset of the snow-melt season occurs earlier than in the observations. The same occurs around Antarctica, where sea-ice draft observations are rather sparse, suggesting too thin sea ice there as well.

4 Discussion and conclusions

We have described the CLIMBER-3α Earth System model and its performance for present-day boundary conditions. The model combines a simplified atmospheric component (POTSDAM-2, the atmospheric module of CLIMBER-2) and a state-of-the-art ocean model, the MOM 3 OGCM, which includes a biogeochemistry component and a state-of-the-art sea-ice model, the ISIS model.

Owing to its relatively simple atmospheric component, CLIMBER-3α is approximately two orders of magnitude faster than coupled AOGCMs, while its oceanic component allows for a larger degree of realism compared to those EMICs which include simpler oceanic components.

The MOM 3 ocean model configuration was set-up following what are considered to be the "best practices" in ocean modelling (Griffies et al. 2000a), and includes a number of new parameterisations and numerical schemes. It uses a non-linear, explicit free-surface which allows incorporating directly changes in ocean volume, parameterisations for spatially variable vertical mixing, including the KPP boundary layer mixing scheme, and a tracer advection scheme that strongly minimises numerical diffusion.

One of the main limitations of the model concerns the simulated surface-wind. The simulated wind-stress is not satisfactory to achieve a realistic oceanic circulation. Thus, we decided to use observed winds plus simulated wind-stress anomalies to force the ocean (Sect. 2.3). Other than that, the model does not include flux corrections. We are working on a new atmospheric model with improved physics and resolution, which we hope will be able to overcome this shortcoming in the future.

Our results show a satisfying agreement with the observations. Errors in SAT and SST (as compared to observed climatologies) are comparable to those of coarse resolution, coupled AOGCMs without flux corrections, which we consider a success given the reduced complexity and much greater computational efficiency of our model.

To account for the uncertainty surrounding the values of abyssal mixing, we created two model versions with different values for the background vertical diffusivity coefficient ($\kappa_v^{bg} = 0.1, 0.4 \times 10^{-4}$ m^2 s^{-1}). As a result of the tracer advection scheme employed, which strongly minimises numerical diffusion, the ocean component simulates the large-scale oceanic circulation with very little explicit vertical diffusion, as shown in the control run with $\kappa_v^{bg} = 0.1 \times 10^{-4}$ m^2 s^{-1}. In particular the main features and the strength of the zonally averaged MOCs, as well as the characteristics of the associated water masses, are simulated satisfactorily. The simulated sea surface elevation captures well the main characteristics seen in the observations (Levermann et al. 2005).

CLIMBER-3α will allow many experiments of multi-millennial duration, and is thus particularly suited to compute climatic equilibrium states or perform long transient experiments. Compared to many models with simpler ocean components, which have been used for this purpose so far (e.g. the CLIMBER-2 model), the main strength of the new model is the realism of its ocean circulation. Compared to ocean-only models or those with a simple energy-balance atmosphere, the new model has the advantage of simulating basic atmospheric circulation features and fundamental feedbacks such as cloud or water vapour feedback. We thus hope this model will be a useful addition to the spectrum of available climate models.

References

Arakawa A (1966) Computational design of long-term numerical integration of the equations of fluid motions. J Comp Phys 1:119–143

Bacon S, Gould WJ, Jia Y (2003) Open convection in the Irminger Sea. Geophys Res Lett 30(5):Art no 1246

Böning CW, Bryan FO, Holland WR, Döscher R (1996) Deep water formation and meridional overturning in a high resolution model of the North Atlantic. J Phys Oceanogr 26:1142–1164

Boris JP, Book DL (1973) Flux-corrected transport I. SHASTA: A fluid transport algorithm that works. J Comp Phys 11:38–69

Bourke RH, Garrett RP (1987) Sea ice thickness distribution in the Arctic Ocean. Cold Regions Sci Technol 13:259–280

Brovkin V, Bendtsen J, Claussen M, Ganopolski A, Kubatzki C, Petoukhov V, Andreev A (2000) Carbon cycle vegetation and climate dynamics in the Holocene experiments with the CLIMBER-2 model. Glob Biogeochem Cyc 16(4):1139. doi: 10.1029/2001GB001662

Bryan K (1969) A numerical method for the study of the circulation of the world ocean. J Comp Phys 4:347–376

Bryan K (1984) Accelerating the convergence to equilibrium of ocean-climate models. J Phys Oceanogr 14:666–673

Claussen M, Mysak LA, Weaver AJ, Crucifix M, Fichefet T, Loutre M-F, Weber SL, Alcamo J, Alexeev VA, Berger A, Calov R, Ganopolski A, Goosse H, Lohmann G, Lunkeit F, Mokhov II, Petoukhov V, Stone P, Wang Z (2002) Earth system models of intermediate complexity: closing the gap in the spectrum of climate models. Clim Dyn 18:579–586

Dickinson RE, Henderson-Sellers A, Kennedy PJ, Wilson MF (1986) Biosphere–atmosphere transfer scheme (BATS) for the NCAR CCM NCAR/TN-275-STR. National Center for Atmospheric Research Boulder Colorado, p 69

Döös K, Webb DJ (1994) The Deacon cell and other meridional cells of the Southern Ocean. J Phys Oceanogr 24:429–442

Emery W, Fowler C, Maslanik J (1997) Satellite-derived maps of Arctic and Antarctic sea ice motion: 1988 to 1994. Geophys Res Lett 24(8):897–900

Fichefet T, Morales-Maqueda MA (1997) Sensitivity of a global sea ice model to the treatment of ice thermodynamics. J Geophys Res 102:12609–12646

Fichefet T, Morales-Maqueda MA (1999) Modelling the influence of snow accumulation and snow-ice formation on the seasonal cycle of the Antarctic sea-ice cover. Clim Dyn 15:251–268

Ganachaud A, Wunsch C (2000) Improved estimates of global ocean circulation heat transport and mixing from hydrographic data. Nature 408:453–457

Gent PR, McWilliams JC (1990) Isopycnal mixing in ocean circulation models. J Phys Oceanogr 20:150–155

Gent PR, Willebrand J, McDougall TJ, McWilliams JC (1995) Parameterizing eddy-induced tracer transports in ocean circulation models. J Phys Oceanogr 25:463–474

Gerdes R, Köberle C, Willerbrand J (1991) The influence of numerical advection schemes on the results of ocean general circulation models. Clim Dyn 5:211–226

Gloersen P, Campbell W, Cavalieri D, Comiso J, Parkinson C, Zwally H (1992) Arctic and Antarctic sea ice 1978-1987: satellite passive-microwave observations and analysis, NASA SP-511

Gnanadesikan A, Toggweiler JR (1999) Constraints by silicon cycling on vertical exchange in general circulation models. Geophys Res Lett 26(13):1865–1868

Goosse H, Fichefet T (1999) Importance of ice-ocean interactions for the global ocean circulation: a model study. J Geophys Res 104(C10):23337–23355

Gregg MC, Sanford TB, Winkel DP (2003) Reduced mixing from the breaking of internal waves in equatorial waters. Nature 422:513–515

Gregory JM, Mitchell JFB (1997) The climate response to CO_2 of the Hadley Centre coupled AOGCM with and without flux adjustment. Geophys Res Lett 24(15):1943–1946

Grenfell T, Maykut G (1977) The optical properties of ice and snow in the Arctic basin. J Glaciol 18:445–463

Grenfell T, Perovich DK (1984) Spectral albedos of sea ice and incident solar irradiance in the Southern Beaufort Sea. J Geophys Res 89:3573–3580

Griffies SM (1997) The Gent-McWilliams skew flux. J Phys Oceanogr 28:831–841

Griffies SM, Boning C, Bryan FO, Chassignet EP, Gerdes R, Hasumi H, Hirst A, Treguier AM, Webb D (2000) Developments in ocean climate modelling. Ocean Model 2:123–192

Griffies SM, Pacanowski RC, Hallberg RW (2000) Spurious Diapycnal Mixing Associated with Advection in a z-Coordinate Ocean Model. Mon Wea Rev 128:538–564

Grist JP, Josey SA (2003) Inverse analysis adjustment of the SOC air-sea flux climatology using ocean heat transport constraints. J Clim 16:3274–3295

Grody NC (1991) Classification of snow cover and precipitation-using the special sensor microwave/imager (SSM/I). J Geophys Res 96(D4):7423–7435

Hansen B, Østerhus S (2000) North Atlantic-Nordic Seas exchanges. Prog Oceanogr 45:109–208

Hansen J, Russell G, Rind D, Stone P, Lacis A, Lebedeff S, Duedy R, Travis L (1983) Efficient three-dimensional global models for climate studies: models I and II. Mon Wea Rev 111:609–662

Harrison EP, Minnis P, Barkstrom BP, Ramanathan V, Cess RD, Gibson GC (1990) Seasonal variation of cloud radiative forcing derived from the earth radiation budget experiment. J Geophys Res 95:18687–18703

Hasumi H, Suginohara N (1999) Effects of locally enhanced vertical diffusivity over rough bathymetry on the world ocean circulation. J Geophys Res 104:23367–23374

Hautala SL, Roemmich DH, Schmitz WJ Jr (1994) Is the North Pacific in Sverdrup balance along 40°N?. J Geophys Res 99:16041–16052

Hibler WD (1979) A dynamic-thermodynamic sea-ice model. J Phys Oceanogr 9:815–846

Houghton JT, Ding Y, Griggs D, Noguer M van der Linden PJ, Xiaosu D (eds) (2001) Climate change 2001: the scientific basis. Contribution of Working Group I to the 3rd assessment report of the intergovernmental panel on climate change (IPCC). Cambridge University Press, Cambridge

Hunke EC, Dukowicz JK (1997) An elastic-viscous-plastic model for sea ice dynamics. J Phys Oceanogr 27:1849–1867

Josey SA (2001) A comparison of ECMWF, NCEP-NCAR, and SOC surface heat fluxes with moored buoy measurements in the subduction region of the Northeast Atlantic. J Clim 14:1789–1789

Josey SA, Kent EC, Taylor PK (1998) The Southampton Oceanography Centre (SOC) Ocean–atmosphere heat momentum and freshwater flux atlas. Southampton Oceanography Centre Report No 6, p 33

Kamenkovich IV, Marotzke J, Stone P (2000) Factors affecting heat transport in an Ocean General Circulation Model. J Phys Oceanogr 30:175–194

Key R, Kozyr A, Sabine C, Lee K, Wanninkhof R, Bullister J, Feely R, Millero F, Mordy C, Peng T-H (2004) A global ocean carbon climatology: results from GLODAP. Glob Biogeochem Cyc 18:4031. doi:10.1029/2004GB002247

Kistler R, Kalnay E, W WC, Saha S, White G, Woollen J, Chelliah M, Ebisuzaki W, Kanamitsu M, Kousky V, van den Dool H, Jenne R, Fiorino M (2001) The NCEP-NCAR 50-year reanalysis: monthly means CD-ROM and documentation. Bull Am Met Soc 82:247–267

Lab Sea Group (1998) The Labrador Sea deep convection experiment. Bull Am Met Soc 79(10):2033–2058

Lambert SJ, Boer GJ (2001) CMIP1 evaluation and intercomparison of coupled climate models. Clim Dyn 17:83–106

Large WG, McWilliams JC, Doney SC (1994) Oceanic vertical mixing: A review and a model with a nonlocal boundary layer parameterization. Rev Geophys 32:363–403

Ledwell J, Watson A, Law C (1993) Evidence for slow mixing across the pycnocline from an open-ocean tracer release experiment. Nature 364:701–703

Ledwell J, Montgomery E, Polzin K, Laurent L, Schmitt R, Toole J (2000) Evidence for enhanced mixing over rough topography in the abyssal ocean. Nature 403:179–182

Leemans R, Cramer W (1991) The IIASA database for mean monthly values of temperature, precipitation and cloudiness of a global terrestrial grid. Research Report RR-91-18 International Institute of Applied Systems Analyses, Laxenburg, Austria

Levermann A, Griesel A, Hofmann M, Montoya M, Rahmstorf S (2005) Dynamic sea level changes following changes in the thermohaline circulation. Clim Dyn 24:347–354

Levitus S (1982) Climatological atlas of the world ocean. NOAA Professional Paper, vol 13. US Dept of Commerce NOAA Washington DC

Manabe S, Stouffer RJ (1988) Two stable equilibria of a coupled ocean-atmosphere model. J Clim 1:841–866

Marshall J, Schott F (1999) Open-ocean convection: observations, theory, and models. Rev Geophys 37:1–64

Massom RA, Eicken H, Haas C, Jeffries MO, Drinkwater MR, Sturm M, Worby AP, Wu XR, Lytle VI, Ushio S, Morris K, Reid PA, Warren SG, Allison I (2001) Snow on Antarctic Sea ice. Rev Geophys 39:413–445

Moum J, Osborn T (1986) Mixing in the main thermocline. J Phys Oceanogr 16:1250–1259

Moum J, Caldwell D, Nash J, Gunderson G (2002) Observations of boundary mixing over the continental slope. J Phys Oceanogr 32:2113–2130

National Geophysical Data Center (1988) Data announcement 88-MGG-02 digital relief of the surface of the earth. National Oceanic and Atmospheric Administration (NOAA), Boulder, CO

Nowlin W, Klinck J (1986) The physics of the Antarctic Circumpolar Current. Rev Geophys 24:469

Oakey N, Ruddick B, Walsh D, Burke J (1994) Turbulence and microstructure measurements during NATRE. Eos 75:130

Opsteegh JD, Haarsma RJ, Selten FM, Kattenberg A (1998) EC-BILT: a dynamic alternative to mixed boundary conditions in ocean models. Tellus 50A:348–367

Pacanowski RC, Griffies SM (1999) The MOM-3 manual. Technical Report 4, GFDL Ocean Group, NOAA/Geophysical Fluid Dynamics Laboratory, Princeton, NJ

Paluszkiewicz T, Romea R (1997) A one-dimensional model for the parameterization of deep convection in the ocean. Dyn Atmos and Oceans 26:95–130

Parkinson C, Cavalieri D, Gloersen P, Zwally H, Comiso J (1999) Arctic sea ice extents areas and trends 1978–1996. J Geophys Res 104(C9):20837

Peixoto J, Oort A (1992) Physics of climate. American Institute of Physics, New York

Petoukhov V, Ganopolski A, Brovkin V, Claussen M, Eliseev A, Kubatzki C, Rahmstorf S (2000) CLIMBER-2: a climate system model of intermediate complexity. Part I: model description and performance for present climate. Clim Dyn 16(1):1–17

Polzin K, Toole J, Ledwell J, Schmitt R (1997) Spatial variability of turbulent mixing in the Abyssal Ocean. Science 276:93–96

Prather MC (1986) Numerical advection by conservation of second order moments. J Geophys Res 91:6671–6681

Rahmstorf S (2002) Ocean circulation and climate during the past 120,000 years. Nature 419:207–214

Rahmstorf S, Ganopolski A (1999) Long-term global warming scenarios computed with an efficient coupled climate model. Clim Change 43:353–367

Redi MH (1982) Oceanic isopycnal mixing by coordinate rotation. J Phys Oceanogr 12:1154–1158

Robbins PE, Toole JM (1997) The dissolved silica budget as a constraint on the meridional overturning circulation of the Indian Ocean. Deep Sea Res 44:879–906

Schlitzer R (2000) Electronic atlas of WOCE hydrographic and tracer data Now Available. Eos Trans AGU 81(5):45

Schott F, Lee T, Zantopp R (1988) Variability of structure and transport of the Florida current in the period range from days to seasonal. J Phys Oceanogr 18:1209–1230

Semtner AJ (1976) A model for the thermodynamic growth of sea ice in numerical investigations of climate. J Phys Oceanogr 6:379–389

Shine K, Henderson-Sellers A (1985) The sensitivity of a thermodynamic sea ice model to changes in surface albedo parameterization. J Geophys Res 2243–2250:2243–2250

Speer K, Rintoul SR, Sloyan B (2000) The diabatic deacon cell. J Phys Oceanogr 30:3212–3222

Stammer D, Wunsch C, Giering R, Eckert C, Heimbach P, Marotzke J, Adcroft A, Hill CN, Marshall J (2002) Global ocean circulation during 1992-1997, estimated fron ocean observations and a general circulation model. J Geophys Res 107:C9 doi: 10.1029/2001JC000888

Stocker TF, Wright DG, Mysak LA (1992) A zonally averaged coupled ocean-atmosphere model for paleoclimate studies. J Clim 5:773–797

Talley L, Reid J, Robbins P (2003) Data-based meridional overturning streamfunctions for the Global Ocean. J Clim 16:3213

Timmermann A, Goosse H (2004) Is the wind-stress forcing essential for the meridional overturning circulation? Geophys Res Lett 31:L04,303. doi: 10.1029/2003GL01,877

Toggweiler JR, Samuels B (1993) New radiocarbon constraints on the upwelling of abyssal water to the ocean's surface. In: Heimann M (ed) The global carbon cycle, NATO ASI Series, Springer

Trenberth KE, Caron JM (2000) Estimates of meridional atmosphere and ocean heat transports. J Clim 14:3433–3443

Weaver AJ, Eby M, Wiebe EC, Bitz CM, Duffy PB, Ewen TL, Fanning AF, Holland MM, MacFadyen A, Saenko O, Schmittner A, Wang H, Yoshimori M (2001) The UVic earth system climate model: model description climatology and applications to past present and future climates. Atmos Ocean 4:361–428

Wijffels SE (2001) Ocean transport of freshwater. In: Ocean circulation and Climate. Academic, New York

Wunsch C, Hu D, Grant B (1983) Mass heat salt and nutrient fluxes in the South Pacific Ocean. J Phys Oceanogr 13:725–753